Materials Horizons

ROYAL SOCIETY OF CHEMISTRY

REVIEW

View Article Online
View Journal

Cite this: DOI: 10.1039/d5mh02484f

Materials- and process-driven microstructural engineering for scalable dry-processed electrode manufacturing

Gwonsik Nam,†[a] Jaejin Lim,†[b] Seungyeop Choi,†[b] Sang Cheol Nam,[c] Kijoo Hong,[d] Jisung Lee[d] and Yong Min Lee *[ab]

Solvent-free dry-processed electrode (DPE) technology has become a promising platform for the manufacturing of lithium-ion batteries, offering a low carbon footprint, enhanced energy efficiency, and cost-effectiveness compared to conventional slurry-based processes. In addition to its process sustainability, the dry process enables the formation of a distinctive electrode microstructure, characterized by a well-interconnected pore network, low tortuosity, a broadened active surface area, and improved electron conduction pathways, which supports high energy density and power performance. Although considerable laboratory-scale progress has been made, several critical challenges, such as the non-uniform binder distribution, insufficient mechanical integrity during large-scale manufacturing, and limitations in current collector compatibility, still hinder the commercialization of DPEs while preserving their microstructural advantages. Overcoming these barriers requires synergistic innovations in terms of materials design and process engineering. This review highlights recent advancements in key material components, including active materials, conductive additives, binders, and current collectors, along with process technologies such as powder mixing, kneading, laminating, and calendering, all from the perspective of microstructural optimization. We discuss how materials innovation can address process limitations and, conversely, how novel process strategies can accommodate material constraints. Finally, this review provides a microstructure-centric perspective on the materials and process innovations required for ensuring the scalable production of high-performance and sustainable DPEs with unique microstructural features.

Received 31st December 2025,
Accepted 20th February 2026

DOI: 10.1039/d5mh02484f

rsc.li/materials-horizons

Wider impact

Owing to the growing interest in gigafactory-scale and sustainable battery manufacturing, dry-processed electrodes (DPEs) have become a promising platform, eliminating toxic solvents and energy-intensive drying processes. This review highlights recent advances in both materials design and process engineering that enable the scalable fabrication of DPEs with structurally robust architectures. Unlike conventional slurry-based electrodes, DPEs have distinctive microstructural features that are not simply determined by the materials or processes alone but are co-shaped through their coupled, bidirectional interplay. These microstructures critically impact electrode performance and reliability, especially in thick electrodes. By characterizing the DPE manufacturing process into four key stages—mixing, kneading, laminating, and calendering—the origin of major defects, including non-uniformity, delamination, and heterogeneous densification, is identified and strategies for mitigating these issues are proposed. This review provides a practical framework linking materials chemistry and process engineering to microstructure and performance, offering valuable insights for researchers and engineers developing the next generation of high-performance, scalable, and sustainable electrode manufacturing technologies.

1. Introduction

The growing urgency to mitigate the impacts of climate change has accelerated the global transition toward electrification, primarily enabled by lithium-ion battery (LIB) technologies. In recent years, the global sale of electric vehicles (EVs) has increased by >24%, highlighting the rapid expansion of the EV market.[1–3] Despite this growth, the practical implementation of EVs remains hindered by inherent trade-offs among core

[a] Department of Battery Engineering, Yonsei University, 50 Yonsei-ro, Seodaemun-gu, Seoul 03722, Republic of Korea. E-mail: yongmin@yonsei.ac.kr
[b] Department of Chemical and Biomolecular Engineering, Yonsei University, 50 Yonsei-ro, Seodaemun-gu, Seoul 03722, Republic of Korea
[c] Cathode Materials Research Center, POSCO Future M, 31 Sojeongsandan 4-ro, Sojeong-myeon, Sejong-si, 30002, Republic of Korea
[d] LIB Materials Research Center, POSCO N.EX.T Hub, POSCO Holdings, 100 Songdogwahak-ro, Yeonsu-gu, Incheon, 21985, Republic of Korea
† These authors contributed equally to this work.

battery attributes, particularly energy density, affordability, and safety, each with stringent and often conflicting requirements. To fully replace internal-combustion engine vehicles, LIBs must simultaneously meet performance targets, including high energy density (>350 Wh kg_{cell}^{-1}), low manufacturing costs (<100 USD kWh_{cell}^{-1}), long-term durability (>15-year service life), and high safety under actual operating conditions.[4–7] These performance demands have driven extensive research on all major battery components, including cathodes, anodes, electrolytes, and separators. Traditionally, LIB development has focused on chemistry-driven materials-level innovation, leading to remarkable advances in terms of intrinsic electrochemical properties such as specific capacity, electrochemical stability, and cycle life.[8–12] While such material-level improvements have resulted in notable performance gains, it is becoming increasingly evident that cell-level performance is not solely determined by chemistry alone. Instead, the architecture of electrodes, including design parameters such as composition, mass loading, and density, and microstructural features like component distribution, active surface area, and ion/electron conduction pathways play decisive roles in translating material properties into real-world device performance. Consequently, studies have recently moved beyond materials design to incorporate electrode- and cell-level engineering, highlighting the need for integrated approaches that optimize materials, structures, and processing in tandem.[13–17]

Among the various electrode-level strategies, the design of thick electrodes is gaining increasing attention as a promising approach for simultaneously reducing the manufacturing cost per kilowatt-hour (kWh) and enhancing the energy density by minimizing the relative fractions of inactive components such as current collectors and separators. For instance, by increasing the cathode mass loading from 20 mg cm^{-2} (roughly equivalent to a thickness of $\sim$57 μm at an electrode density of 3.5 g cm^{-3}) to 70 mg cm^{-2} ($\sim$200 μm), the proportion of inactive components could be reduced from approximately 21% to 6%, while the gravimetric energy density could be increased from 475 Wh kg^{-1} to 541 Wh kg^{-1} (this estimation considered only the cathode and current collector).[18–20] Despite these advantages, conventional wet-processed electrodes (WPEs) face intrinsic limitations when implemented in thick formats. Solvent evaporation during drying often induces problems such as carbon–binder domain (CBD) migration and electrode delamination, leading to structural heterogeneity and increased internal resistance.[21–23] Additionally, wet processing depends on energy-intensive drying and toxic solvent recovery systems (*e.g.*, *N*-methyl-2-pyrrolidone, NMP), thereby increasing both manufacturing costs and environmental burdens.

To overcome these limitations, dry-processed thick electrodes, which eliminate the need for solvents and the associated drying and recovery processes, have been adopted. By avoiding solvent-related emissions and substantially lowering energy consumption, dry-processed electrodes (DPEs) offer a significantly reduced carbon footprint.[24]

While dry process techniques provide distinct advantages, the comprehensive understanding of how materials selection and processing strategies co-shape the electrode microstructure in DPEs remains limited. This review critically examines recent advances in DPE technology by integrating materials innovation and process engineering within a microstructure-centric framework. This approach underscores the bi-directional interplay between materials and processes, highlighting how targeted materials design can mitigate the intrinsic limitations of processes, and, conversely, how advanced processing strategies can accommodate material constraints.

Key electrode components, including active materials, conductive additives, binders, and current collectors, are systematically discussed, alongside critical processing steps such as powder mixing, kneading, laminating, and calendering, with particular emphasis on how materials innovation and processing strategies result in microstructure evolution in DPEs. Furthermore, polytetrafluoroethylene (PTFE)-based binder systems, which continue to play a central role in DPE manufacturing, are examined, alongside emerging alternatives that present new opportunities for microstructural control and functional enhancement in DPEs. Ultimately, this review provides a unified, microstructure-driven perspective that bridges materials chemistry with process design, offering critical insights into the scalable manufacturing of high-performance, cost-effective, and environmentally sustainable DPEs.

2. Advantages and manufacturing methods of dry-processed electrodes

2.1. Advantages of the dry process, compared to the conventional slurry-based wet process

2.1.1. Environmental sustainability and cost-effectiveness. Fig. 1a schematically illustrates the conventional slurry-based wet electrode manufacturing process, which typically involves four main steps: (1) slurry mixing, (2) slurry coating, (3) drying, and (4) calendering. A solvent recovery system is also required to regenerate toxic organic solvents such as NMP, which are widely used in cathode slurries. In commercial-scale production, the drying process and recovery step are particularly energy-intensive, accounting for 46.84% of the total energy consumed for full-cell manufacturing. To precisely control the drying temperature and solvent evaporation rate, a multi-zone drying system is employed, often extending over 100 m and consisting of dozens of sequential convection ovens regulated at temperatures ranging from tens to several hundreds of degree Celsius.[24–26] To recover evaporated NMP, large-scale purification units incorporating multi-stage distillation columns are used. Notably, such recovery systems consume up to 230 kW for operating blowers and exhaust fans alone. Moreover, the energy required to recover 1 kg of NMP can reach about 10 kWh, approximately 45 times higher than the latent heat of vaporization for pure NMP, owing to the need to heat and circulate large volumes of air to prevent explosion hazards.[27,28] This combination of extensive drying infrastructure and energy-demanding solvent recovery increases both the capital expenditure (CAPEX) and operational expenditure

(OPEX), contributing to the total manufacturing cost and carbon footprint of WPEs. In contrast, DPEs, shown schematically in Fig. 1b, eliminate the need to use solvents and the associated drying and recovery stages altogether. For instance, PTFE-based DPEs use the fibrillation behavior of PTFE under shear stress, enabling a streamlined fabrication route consisting of (1) powder mixing, (2) kneading, (3) sheet forming, and (4) laminating and calendering.[29–31] This approach eliminates the need for drying and solvent recovery and reduces the overall process complexity. Consequently, DPEs can reduce the number of equipment units required by up to 30% and decrease both CAPEX and OPEX by approximately 20%. Moreover, by removing the drying bottleneck, the speed of electrode coating can be increased by up to 20%. From a sustainability perspective, conventional WPE production emits approximately 2.3 kg CO_2 per kWh of electrode capacity, whereas the dry process has been reported to reduce these emissions by up to 60% (Fig. 1c and d).[30,32–36]

2.1.2. Electrode microstructure. The electrochemical performance of LIBs is governed not only by the intrinsic properties of the constituent materials but also by the microstructure of the electrodes. Critical microstructural features include the spatial distribution and morphology of each component, interfacial contact between active materials and CBDs, effective surface area for interfacial electrochemical reactions, tortuosity of ion percolation pathways, and continuity of electronic conduction networks. These features collectively determine key performance metrics such as rate capability, cycle life, energy density, and safety.[16,22,37–39] Notably, by eliminating solvent usage and the drying step, DPEs offer distinct advantages in terms of electrode microstructure, compared to WPEs. As shown in Fig. 1e, the drying process in WPEs often causes CBD migration, resulting in the formation of non-uniform CBDs, especially in the thickness direction. These bulky CBD agglomerates obstruct lithium-ion pathways and increase tortuosity, thereby impeding ion transport and worsening rate performance.[40–42] In contrast, DPEs with PTFE binders benefit from the polymer's fibrillation under shear during overall mixing processes, which form a continuous fibrillar network. This network minimizes pore blockage, facilitating the establishment of well-connected lithium-ion conduction pathways and improving rate capability.[15] Remarkably, this fibril network enables the fabrication of self-standing electrodes with binder contents as low as 1 wt%, significantly reducing the proportion of electrochemically inactive components and improving the overall energy density. Moreover, in thick electrodes, WPEs are more susceptible to structural inhomogeneities such as edge elevation (in-plane non-uniformity), through-plane CBD migration, and drying-induced cracking or delamination. These issues are inherently mitigated in DPEs, owing to their solvent-free fabrication. Therefore, DPEs are particularly well-suited for the construction of thick, high-loading electrodes, offering superior microstructural uniformity and mechanical stability.[20]

2.2. Typical manufacturing methods for dry-processed electrodes

Various manufacturing methods have been developed for DPEs, including PTFE-fibrillation-based methods (Maxwell technology),[43,44] powder hot pressing,[45,46] melting extrusion,[47,48] vapor deposition,[49] dry-spray deposition,[50–52] and 3D printing.[53] Among these, Maxwell/PTFE fibrillation, melting extrusion, and spray deposition demonstrate the highest technological maturity and scalability, especially in terms of roll-to-roll (R2R) compatibility and industrial applicability. Fig. 1f provides a comparative schematic overview of these representative dry fabrication methods.

2.2.1. Maxwell/PTFE fibrillation. The PTFE-fibrillation-based (Maxwell) method is the most widely implemented strategy for DPE fabrication, with successful demonstrations ranging from lab-scale prototyping to commercial mass production.[43,44] This method utilizes the unique fibrillating behavior of PTFE under mechanical shear stress to create an interconnected fibrous binder network that physically entangles and binds active materials and conductive additives without requiring solvents.[54] First, PTFE powder, active material, and a conductive additive undergo dry mixing to ensure a uniform distribution. Commonly used equipment for this step includes planetary mixers, ball mills, or high-energy shear mixers.[30] Subsequently, the blended powder is fed into a kneader, where the PTFE undergoes fibrillation. Key processing parameters, including the shear rate, temperature, and kneading time, must be strictly controlled to ensure the formation of a robust 3D PTFE fibrillar network.[55,56] The resulting dough-like composite or partially formed dry sheet is then laminated onto a current collector (typically primer-layer-coated Cu or Al foil). Final densification is achieved through additional roll pressing and calendering, during which time the electrode thickness, density, and mass loading can be precisely controlled. Notably, this method enables the fabrication of free-standing or ultra-thick electrodes with high mechanical integrity even at binder contents below 1 wt%, offering remarkable advantages for high-energy-density designs.[15,57]

2.2.2. Melting extrusion. In the melting extrusion method, a mixture of thermoplastic polymer binders, active materials, and conductive additives is processed through a heated extruder.[47,48,58] Inside the extruder, the polymer binder melts, binds the powder constituents, and simultaneously undergoes mixing and shear-induced homogenization. Typical thermoplastic binders, such as polyvinylidene fluoride (PVdF),[46] poly(vinylidene fluoride-*co*-hexafluoropropylene) (PVdF-HFP), poly(ethylene oxide) (PEO),[59] polypropylene (PP),[60] paraffin wax, and polyaniline,[61] can be used in the melting extrusion technique. After extrusion, the composite is formed into sheets *via* hot pressing and then laminated onto a current collector and calendered. This technique is particularly suitable for applications requiring a higher binder content, such as mechanically flexible architecture. However, melting extrusion poses challenges for conventional LIB electrodes that require a low binder content (<2 wt%). At such low loadings, achieving a uniform binder distribution and sufficient mechanical adhesion by employing the melting-extrusion method is difficult. Therefore, precise control over the binder particle size, shear rate, extrusion temperature, and residence time is essential for ensuring good processability and performance.[62]

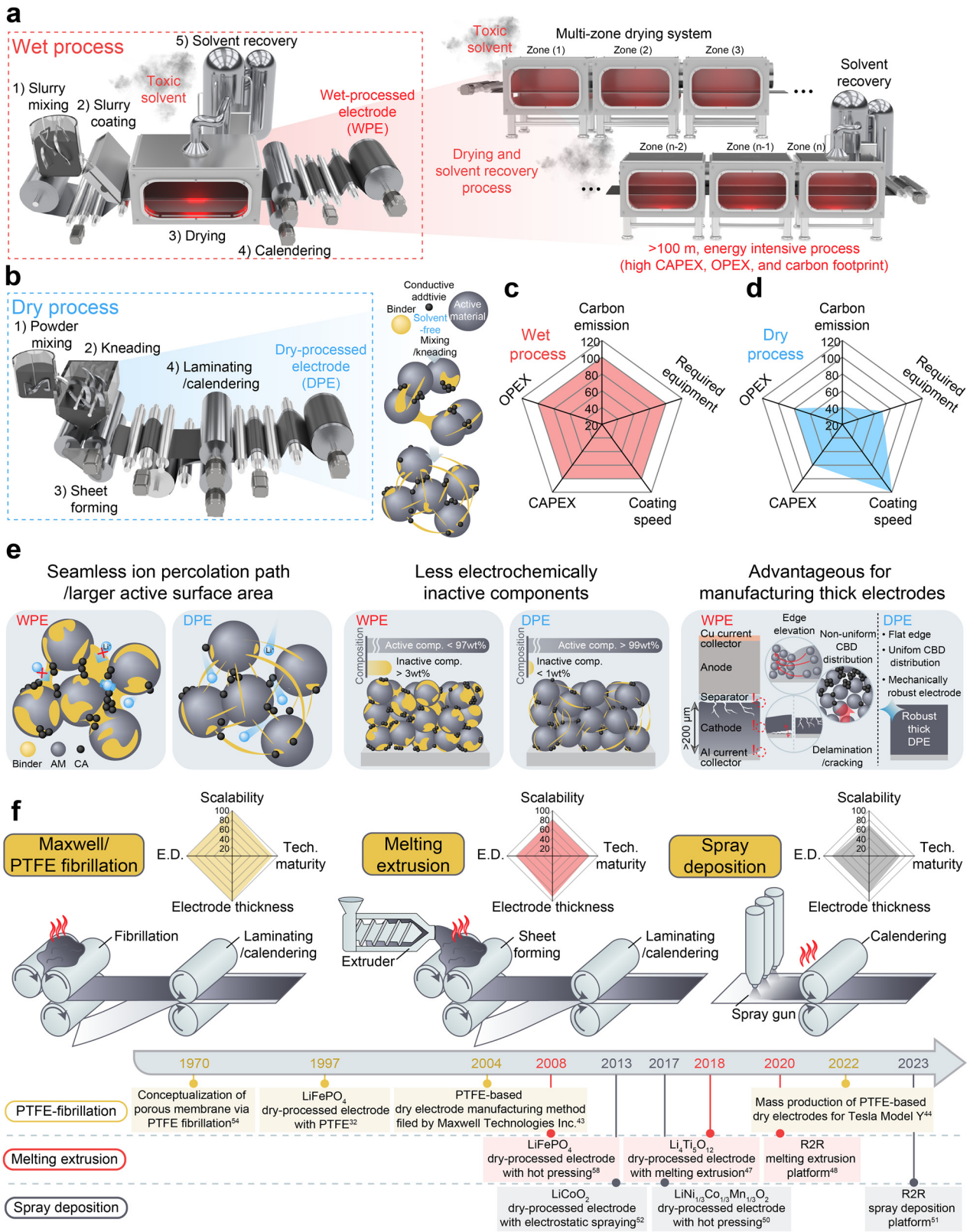

Fig. 1 Schematic illustration of (a) the conventional slurry-based wet process and (b) the dry process for manufacturing LIB electrodes. Radar plots comparing key manufacturing metrics—required equipment, OPEX, CAPEX, coating speed, and carbon emission (each metric normalized to 100% for the wet process)—for (c) the wet process and (d) the dry process. (e) Representative microstructural features and advantages of DPEs over WPEs. (f) Schematic overview, radar plots of the technical features (scalability, technological maturity, electrode thickness, and electrode density (E.D.)), and historical development of typical manufacturing methods for DPEs.

2.2.3. Spray deposition. Spray deposition involves forming DPEs by delivering granulated dry powder blends (typically containing active material, binder, and conductive additive) onto a current collector surface *via* an air- or gas-driven spray nozzle.[50,51] Electrostatic spraying techniques can be used to improve deposition uniformity and adhesion.[63] Following deposition, the electrode undergoes hot-roll pressing to melt or fuse the binder (*e.g.*, thermoplastic or wax-type binders), followed by calendering for further densification and adhesion enhancement. In some cases, post-deposition curing steps, such as thermal annealing or UV crosslinking, may be introduced to enhance the mechanical robustness and cohesion of the electrode layer.[64] This method is highly compatible with R2R production lines owing to its continuous and scalable nature. However, it presents considerable challenges related to the precise control of powder-granule morphology, flow behavior, spray uniformity, and layer thickness.[31] These difficulties can result in uneven mass loading, poor adhesion, or inconsistent porosity across the electrode width. Fig. 1f summarizes the historical evolution and technological progress of the three core DPE manufacturing methods. For each, representative milestones including pioneering studies, subsequent process optimization, and recent advancements toward R2R implementation and commercial-scale deployment are presented. To facilitate a rapid and practical comparison of DPE manufacturing methods, we additionally include a radar chart technical summary in Fig. 1f, highlighting their relative scalability, technological maturity, achievable electrode thickness, and energy density potential based on previous literature studies.[31,152,153]

2.3. Materials- and process-driven dry-processed electrode engineering

As summarized in Fig. 2, several types of microstructural defects can be observed in DPEs, including (1) non-uniformity, (2) delamination, and (3) heterogeneous densification accompanied

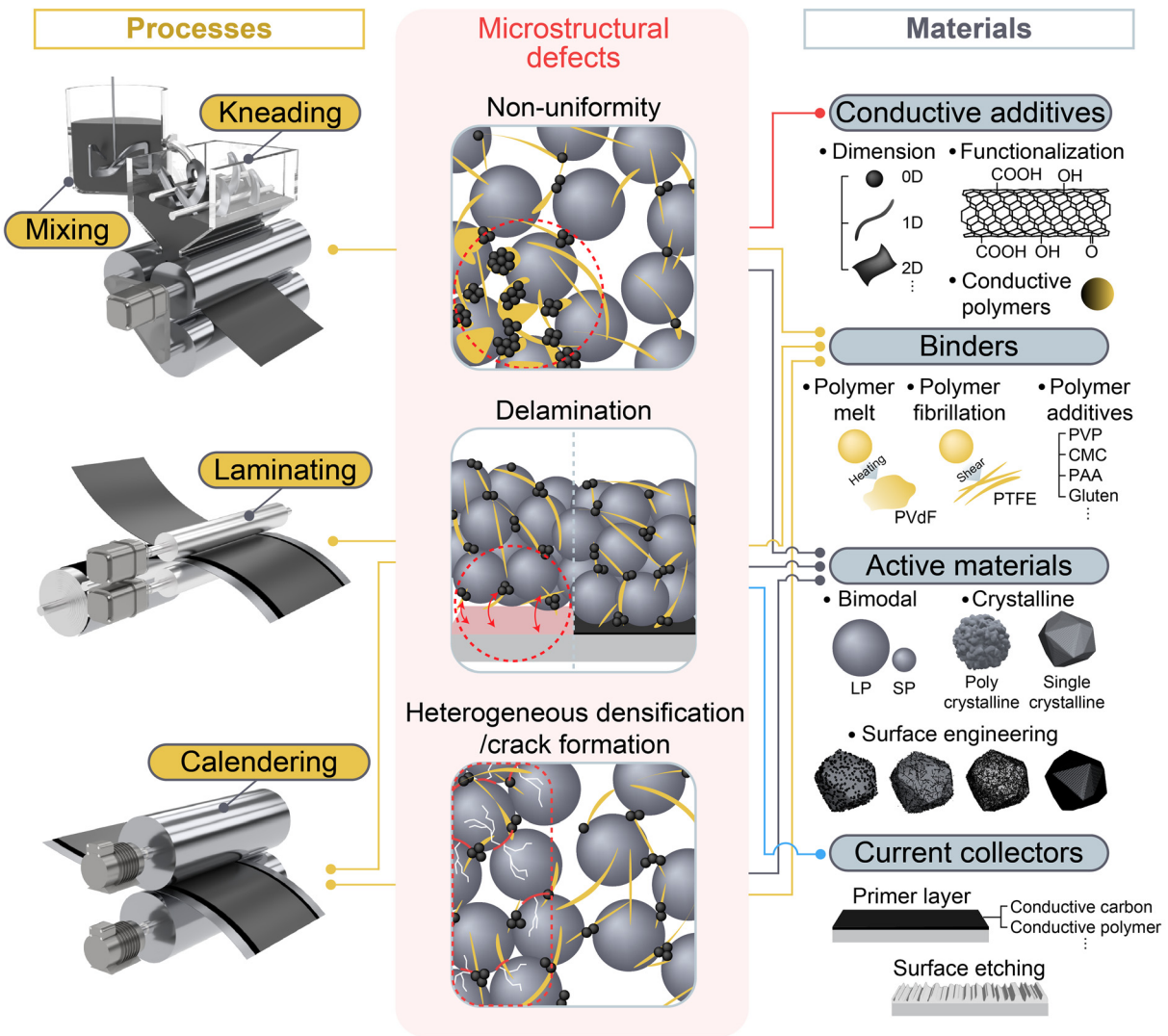

Fig. 2 Microstructural challenges in DPE manufacturing and the interplay between manufacturing processes and materials design.

by crack formation. These issues arise from the complex interplay between processing conditions and material properties. For instance, a non-uniform distribution of components may result from improper shear conditions during mixing and kneading, while also being strongly affected by the particle size, morphology, surface chemistry, and thermodynamic properties of the active materials, conductive additives, and binders. This review dissects the DPE manufacturing process step-wise, including the mixing, kneading, laminating, and calendering processes, and critically examines the microstructural challenges that arise at each stage. We then discuss both process-level modifications and material-level innovations proposed in recent studies to mitigate these issues.

3. Challenges and strategies for scalable dry-processed electrode manufacturing

PTFE-based DPEs are typically dry-mixed and fibrillated before lamination and calendering.[30,55,65] Dry powder mixing strongly affects the microstructure of the resulting powder mixture, thus greatly influencing the electrochemical performance and mechanical integrity of the electrode. Owing to the absence of a dispersing solvent, achieving a homogeneous distribution of electrode components at the microscale remains a critical challenge in dry processing. Moreover, the shear-induced fibrillation of PTFE under mechanical mixing conditions contributes to the formation of a fibrous binder network that enhances mechanical robustness but requires a careful optimization of processing parameters. Finally, because of the hydrophobic nature of PTFE, an optimized lamination strategy is required to address interfacial adhesion issues, while careful control of calendering conditions is essential for mitigating particle microcracking in thick electrodes. The following sections systematically discuss recent strategies involving materials modification and processing control, to overcome the inherent challenges of each step.

3.1. Powder mixing process

The powder mixing process is an important step for ensuring uniform dispersion of active materials, conductive additives, and binders. This process must be achieved through mechanical mixing, as the dispersant-assisted wet dispersion of conductive additives is not employed.[66–69] In terms of material properties, carbon additives are inherently highly likely to agglomerate owing to the presence of van der Waals and π–π interactions as well as because of their high surface energy, making effective dispersion particularly challenging.[57,70,71]

Oh *et al.*[56] reported the effects of various carbon additives on DPEs. Carbon nanotubes (CNTs) exhibited intrinsically high electrical conductivity ($\sim$200 S cm^{-1}), approximately 100 times higher than that of conventional carbon black (Super P: $\sim$29.6 S cm^{-1}, Ketjen black: $\sim$23.2 S cm^{-1}). However, despite this superior intrinsic conductivity, their electrode-level advantage was substantially diminished due to poor dispersion of CNTs under physical mixing conditions. In contrast, conventional carbon black, despite its inherent tendency toward aggregation, showed comparatively more homogeneous dispersion than CNTs owing to its 0D morphological properties. To exploit their intrinsically high electrical conductivity and fibrous morphology, recent efforts focused on achieving homogeneous CNT dispersion, which enables the formation of a percolated electronic network.[154–156] Accordingly, the surface modification strategies have been introduced, offering two key advantages: (1) reducing interparticle agglomeration; the surface functionalization introduces polar functional groups that weaken van der Waals attraction[157,158] and (2) improving interfacial interactions with active materials due to hydrogen bonding and dipole–dipole interactions between active materials and carbon additive surfaces.[57] However, most functionalization approaches rely on acid-based treatments, which often induce buckypaper-like structures, as CNTs inevitably undergo re-bundling during drying due to capillary forces, thereby limiting their dispersibility.[159,160] This limitation becomes more pronounced during dry mixing, as even high shear stress is insufficient to disrupt re-bundled CNTs, ultimately hindering uniform CNT distribution. To mitigate the intrinsic limitations of carbon materials, Kim *et al.*[72] introduced ozone-treated CNTs as shown in Fig. 3a. Conventional CNT functionalization is typically achieved using strong liquid-phase oxidants to generate surface functional groups. However, such an approach often causes severe damage to the sp^2 carbon framework, leading to deterioration of electronic conductivity. In addition, acid-based mixing generally results in the formation of rigid buckypaper structures, making it unsuitable for dry processes. Contrastingly, ozone treatment not only preserves the initial fluffy powdery texture of CNTs but also introduces oxygen-containing functional groups, such as hydroxyl, carbonyl, and carboxylic-acid groups, onto the surface. X-ray microscopy (XRM) analysis revealed that, after pressing, an ozone-treated single-walled CNT (O-SWCNT) electrode with NCM-based cathode active materials maintained a porosity of 13.89%, whereas a Super P-NCM (SP) electrode retained a higher porosity of 20.90%. This difference was attributed to the partial aggregation of Super P particles, even under the application of high shear forces during calendering. As an alternative strategy, the pre-dispersion of carbon materials has been achieved by coating the active materials, rather than by directly modifying the carbon materials themselves.[57,65,73] Koo *et al.*[57] reported a uniform wrapping of a multi-walled CNT (MWCNT) on single-crystalline NCA (SC-NCA) cathode active materials, in which an anti-solvent-induced salt-out effect was employed to trigger MWCNT precipitation (Fig. 3b). In comparison, a conventional WPE containing 2 wt% carbon black (CB-wet) exhibited a highly non-uniform distribution of conductive additives relative to a DPE incorporating CNTs (CNT-Dry). This inhomogeneous conductive network resulted in the degradation of the electronic percolation pathway and, consequently, higher local resistance, as was clearly visualized using 2D scanning spreading resistance microscopy (2D-SSRM). Furthermore, 3D digital twin structural analysis revealed that the effective electronic

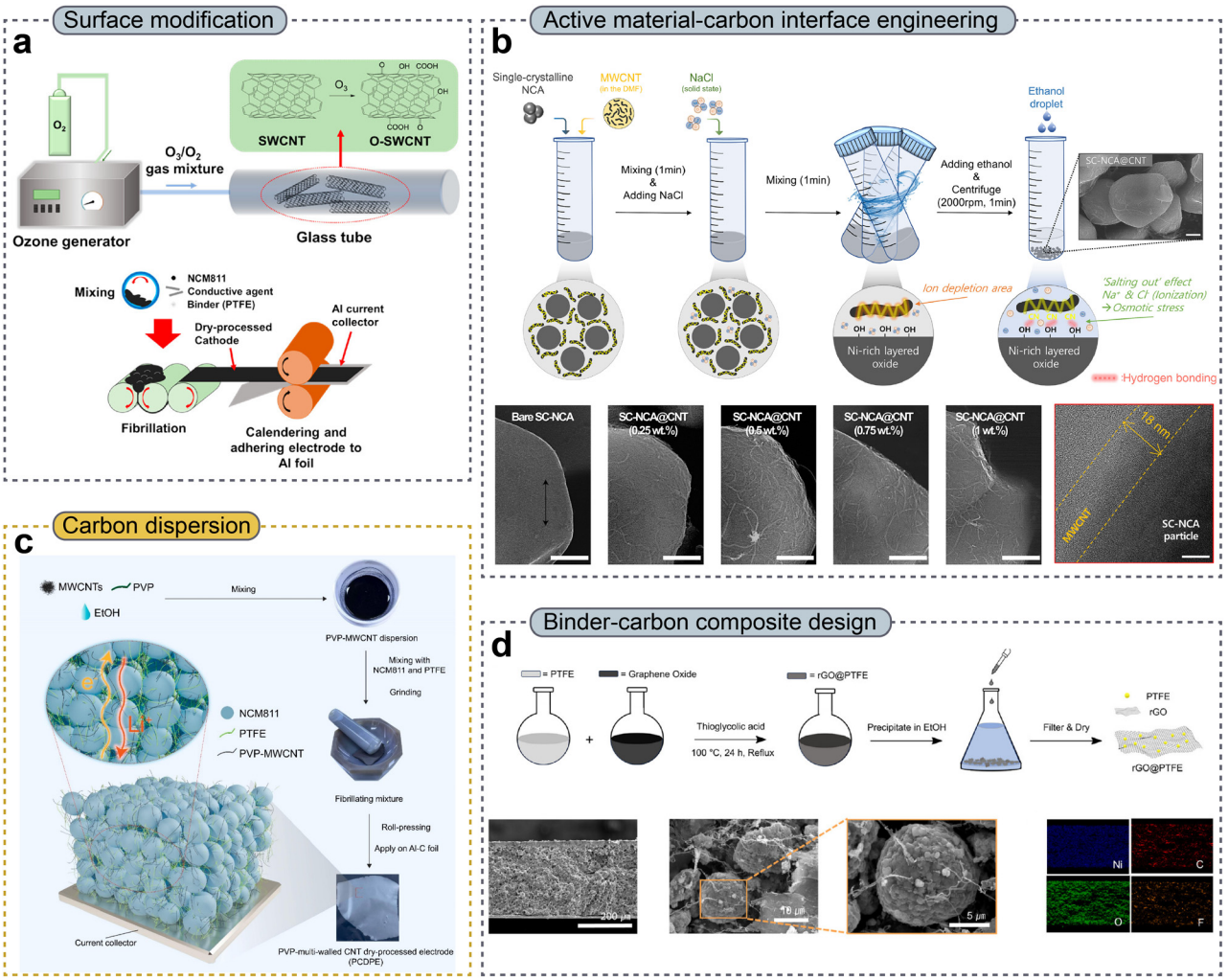

Fig. 3 (a) Schematic illustration of the ozone treatment process for surface functionalization. Reproduced with permission from ref. 72. Copyright 2023, The Royal Society of Chemistry. (b) Processing schematic of MWCNT wrapping on SC-NCA (top) and corresponding SEM and TEM images (bottom). Reproduced with permission from ref. 57. Copyright 2025, Elsevier B.V. (c) The PVP–MWCNT coating process for improving MWCNT dispersibility. Reproduced with permission from ref. 74. Copyright 2025, Elsevier B.V. (d) Schematic procedure of the PTFE coating strategy on rGO (top) and SEM/EDS analyses of electrodes fabricated using rGO@PTFE (bottom). Reproduced with permission from ref. 79. Copyright 2025, Wiley-VCH GmbH.

conductivity ($\sigma_{s,eff}$) of a CNT-DPE was approximately 3.1 times higher than that of a CB-WPE, while the tortuosity of the electronic transport pathways was reduced by 36%. By pre-dispersing an MWCNT directly onto the cathode active material, CNT agglomeration was effectively mitigated, leading to a highly uniform carbon distribution. Consequently, both lithium-ion and electronic transport processes were significantly enhanced, allowing an exceptionally high active material fraction of up to 99.6 wt% within the electrode and achieving a high electrode density of 4.0 g cm^{-3}. Moreover, Linh *et al.*[74] proposed a facile pre-dispersion strategy using polyvinylpyrrolidone (PVP), a cost-effective and widely used polymeric dispersant, to facilitate homogeneous MWCNT dispersion (Fig. 3c). The PVP macromolecular chains absorbed onto the MWCNT surfaces, preventing aggregation and forming a stable dispersion in ethanol before electrode fabrication. The authors achieved a well-distributed conductive network that promoted effective electronic percolation in the electrode. Accordingly, PVP–MWCNT DPEs (PCDPEs) with areal capacities of 8 and 10 mAh cm^{-2} exhibited markedly higher discharge capacity and improved capacity retention than those of MWCNT-only DPEs (CDPEs), highlighting the advantages of enhanced conductive network formation in thick electrodes.

However, the above-mentioned strategies have primarily focused on carbon additives only, whereas achieving a uniform distribution of both carbon additives and binders remains a critical design consideration. Because PTFE is electrically insulating, its inhomogeneous dispersion can induce not only a heterogeneous current density but also deterioration of the mechanical integrity of the electrode structure.[75–77] Accordingly, the spatial distribution of the CBD plays a decisive role in determining both the electronic percolation network and the mechanical robustness of the electrode, thus significantly influencing the overall electrochemical performance.[21–23,78]

Yoon *et al.*[79] reported a wet-chemical process using thioglycolic acid to synthesize a PTFE-nanoparticle-anchored reduced graphene oxide (rGO@PTFE) composite (Fig. 3d). Owing to the presence of anchored PTFE nanoparticles, the rGO@PTFE composite effectively suppressed restacking of rGO sheets, mitigated aggregation, and promoted enhanced nanofibrillation behavior. As a result, the rGO@PTFE-based ultra-thick cathode (G@P_TC) exhibited a high lithium-ion transference number of 0.73, whereas the Super P-PTFE-based thick cathode (S-P_TC) showed a substantially lower value of 0.43. The improved lithium-ion transport in G@P_TC effectively alleviated concentration polarization in thick electrodes, enabling a more uniform ionic flux throughout the electrode. In addition, G@P_TC delivered superior electrochemical performance, achieving a maximum areal capacity of 15.2 mAh cm^{-2} and a volumetric capacity of 563 mAh cm^{-3}, respectively, along with excellent rate capability and cycling stability.

In conclusion, achieving a homogeneous dispersion of inactive materials is critically important, as it determines the electrode microstructure and cell performance. To facilitate a systematic comparison, Table 1 summarizes various strategies for achieving a uniform dispersion of inactive components, including conductive carbon additives and binders.[57,65,72–74,79–81] This comparison provides insights into how the targeted modification of inactive materials can promote uniform mixing behavior, thereby facilitating the scalable fabrication of thick DPEs.

3.2. Kneading process

Kneading is an essential step for PTFE-based DPE processing, as it induces PTFE fibrillation. Apart from ensuring the homogeneous distribution of PTFE, the degree of fibrillation strongly determines the electrode microstructure and mechanical properties, thus considerably influencing electrochemical performance.[82–84] Therefore, from both the perspectives of the intrinsic PTFE properties and processing conditions, systematic studies are required to elucidate how PTFE fibrillation evolves and how the resulting changes influence electrochemical behavior.

Lee *et al.*[76] systematically investigated the mechanical and electrochemical properties of electrodes with respect to the particle size of PTFE (Fig. 4a). Pristine PTFE (PTFE(L)) exhibited an average particle size of 492.31 μm, which decreased to 87.73 μm after 8 cycles of cryogenic freezer milling (CFM, PTFE(M)), and further to 6.44 μm after 16 CFM cycles (PTFE(S)). DPEs fabricated using PTFE with different particle sizes were evaluated using a surface and interfacial cutting analysis system (SAICAS) to assess interfacial adhesion, revealing distinct differences in adhesion behavior between PTFE(L) and PTFE(S) under both vertical and horizontal stresses at a 75% depth. Electrochemical impedance spectroscopy (EIS) analysis further demonstrated that decreasing the PTFE particle size led to reduced charge transport resistance, resulting in enhanced ionic and electronic conductivity. This improvement was attributed to the minimized contact area of the inherently insulating PTFE when employing smaller particles, which facilitated more efficient charge transport within the electrode. As shown in Fig. 4b, Lee *et al.*[85] investigated how molecular weight (M_W) influences the PTFE binder's fibrillation behavior. Compared with low-M_W PTFE (PTFE(L)), high-M_W PTFE (PTFE(H)) exhibited a lower degree of agglomeration and a more uniform fibrous morphology. This behavior stemmed from the sufficiently long polymer chains of PTFE(H), which could sustain and propagate fibril formation, thereby promoting effective fibrillation. Consequently, PTFE(H) showed superior fibrillation behavior and a more homogeneous distribution within the electrode. Composite cathode electrodes incorporating PTFE(H) not only exhibited lower electronic resistance but also demonstrated enhanced adhesion strength. Accordingly, an all-solid-state Li–In/LPSCl/NCM cell employing PTFE(H) delivered a high discharge capacity of 209.7 mAh g^{-1} and exhibited excellent cycling retention of 97.4% after 300 cycles, even at a high mass loading of 22.5 mg cm^{-2}. Furthermore, Lee *et al.*[86] tuned the degree of crystallinity of PTFE by heating it to 200 °C and then varied the cooling rate between 2 and 15 °C min^{-1}. Thereafter, they applied crystallinity- controlled PTFE to compose cathode electrodes for all-solid-state batteries. The prepared PTFE samples with different crystallinities were characterized using X-ray diffraction (XRD), which confirmed the presence of amorphous (A-PTFE), semi-crystalline (SC-PTEF, conventional PTFE), and highly crystalline states (C-PTFE). Stress–strain measurements revealed that A-PTFE resulted in an increased mechanical strength; this enhanced strength effectively mitigated interparticle contact loss within the electrode. In electrochemical evaluations, a C-PTFE adopted NCM cathode electrode exhibited a high initial discharge capacity of 171 mAh g^{-1} and maintained a high capacity retention of 84.1% after 200 cycles. In summary, the intrinsic properties of PTFE, including its M_W, particle size, and crystallinity, are critical in governing the degree of fibrillation and, consequently, the electrochemical performance.

From a processing perspective, the degree of fibrillation varies with kneading parameters such as kneading time, temperature, and feeding steps, thus influencing both the mechanical integrity of electrodes and the ion percolation pathways. Oh *et al.*[55] reported that the fibrillation morphology evolved markedly with kneading time (Fig. 4c). During the initial 5 min of kneading, fibrillation was initiated, while nearly complete fibrillation was achieved at 20 min. In contrast, prolonged kneading for 60 min resulted in an over-kneaded state, in which the fibrils were fractured, leading to a loss of mechanical integrity within the mixer. For F-104 and F-208 binders, although their intrinsic material properties, such as particle size, bulk density, and specific gravity, were comparable, their extrusion ratios differed significantly, ranging from 36 to 1500. During kneading, F-104, which had a lower extrusion ratio, exhibited a higher kneading torque than F-208. These observations highlight the fact that the optimal kneading process must be carefully tailored to the intrinsic properties of the PTFE binder. Moreover, Kim *et al.* reported that temperature is a critical processing factor during PTFE kneading (Fig. 4d).[77] When fibrillation was conducted at 30 °C, insufficient

Table 1 Summary of strategies for mitigating agglomeration of carbon additives and binders

					Electrode composition (wt%)			Electrochemical performance							
Materials		Surface modifier	Function	Approach	Active material	Conductive additive	Binder	Cell configuration	Loading level (mg cm^{-2})	Areal capacity (mAh cm^{-2})	Electrolyte	Voltage range	C-rate@ temperature	Capacity retention@ cycles	Ref.
Active materials	Single crystalline $LiN_{i0.8}Co_{0.1}$-$5Al_{0.05}O_2$	MWCNT	(1) Homogeneous carbon distribution on cathode materials (2) Spatially uniform conductive pathways (3) Enhanced electrode density (4.0 g cm^{-3}) with a low binder composition (0.4 wt%)	Salt-induced selective precipitation method	99.6[NCA/MWCNT = 99.25/0.75(w/w)]	—	0.4(PTFE)	Graphite||NCA	23(NCA)	4.6	1.15 M $LiPF_6$ EC/EMC/DEC 2/4/4 (v/v/v) 1 wt% VC 1 wt% $LiPO_2F_2$	2.5–4.25 V	0.5C@ 25 °C	95%@ 250 cycles	57
	Single crystalline $LiNi_{0.8}Co_{0.1}$-$Mn_{0.1}O_2$	MWCNT	(1) Ultralow binder content (~0.3 wt%) (2) Strong CNT–PTFE interfacial anchoring (3) 3D conductive network with improved tensile strength	Pickering emulsion-assisted assembly method	99.5[NCM811/MWCNT = 99.7/0.3(w/w)]	—	0.5(PTFE)	Graphite+Si||NCM811	51.9 (NCM811)	10	1.1 M $LiPF_6$ EC/DMC/EMC 2/6/2 (v/v/v) 1 wt% VC 10 wt% FEC	3.0–4.3 V	0.33C	78%@ 500 cycles	65
	Single crystalline $LiNi_{0.8}Co_{0.1}$-$Mn_{0.1}O_2$	SWCNT	(1) Homogeneous carbon distribution on cathode materials (2) Ultralow carbon additive content (0.12 wt%)	Spray-drying-assisted composite formation method	98 [NCM811/SWCNT = 99.88/0.12(w/w)]	—	2(PTFE)	Graphite+Si||NCM811	36(NCM811)	7	1 M $LiPF_6$ EC/DMC 3/7 (v/v) 5 wt% FEC	2.5–4.25 V	1.0C	89.40%@ 100 cycles	73
Binder materials	PTFE	Graphene oxide	(1) Lowered percolation threshold (2) Reduced interfacial contact between	Chemical reduction–precipitation method	90(NCM)	—	10[PTFE/rGo = 3/7(w/w)]	Li metal||NCM	85(NCM)	15.2	1 M $LiPF_6$ EC/DMC 1/1 (v/v)	2.7–4.3 V	0.1C	82%@ 100 cycles	79

Table 1 (*continued*)

Materials		Surface modifier	Function	Approach	Electrode composition (wt%)			Electrochemical performance							Ref.
					Active material	Conductive additive	Binder	Cell configuration	Loading level (mg cm^{-2})	Areal capacity (mAh cm^{-2})	Electrolyte	Voltage range	C-rate@ temperature	Capacity retention@ cycles	
			carbon additives and active materials												
	PTFE	MWCNT	(1) Good percolating network (2) Homogeneous electron transport (3) Improved mechanical properties	Freeze-drying-induced composite formation method	98(LCO)	—	2[PTFE/MWCNT = 1/2(w/w)]	Li metal||LCO	101(LCO)	14.8	1 M $LiPF_6$ EC/DMC 1/1 (v/v)	3.0–4.3 V	0.1C	92.60%@20 cycles	80
	PTFE	Carbon black	(1) Preventing agglomeration of the conducting agent and PTFE binder in the electrode	Charge-induced electrostatic assembly method	98(NCMA)	1(Super P)	1[PTFE/Super P = 1/1(w/w)]	Graphite||NCMA	24(NCMA)	5	1.15 M $LiPF_6$ EC/EMC/DEC 2/4/4 (v/v/v) 1 wt% VC 1 wt% $LiPO_2F_2$	2.8–4.3 V	0.5C	82%@200 cycles	81
Conductive additives	SWCNT	—	(2) Increased surface hydrophilicity of carbon additives with decreased electrical conductivity (3) Homogeneous distribution of carbon additive	Ozone-induced surface modification method	96(NCM811)	2(O-SWCNT)	2(PTFE)	Graphite||NCM811	30(NCM811)	5.76	1 M $LiPF_6$ EC/DEC 1/1 (v/v) 10 wt% FEC	2.5–4.25 V	0.33C	85.60%@100 cycles	72
	MWCNT	PVP	(1) Homogeneous distribution of carbon additive (2) Improved charge transfer	Solvent-assisted predispersion method	97(NCM811)	1[MWCNT/PVP = 10/1 (w/w)]	2(PTFE)	Li metal||NCM811	40(NCM811)	8	1 M $LiPF_6$ EC/DMC/EMC 1/1/1 (v/v/v) 1 wt% VC	2.8–4.4 V	0.33C@25 °C	60.23%@50 cycles	74

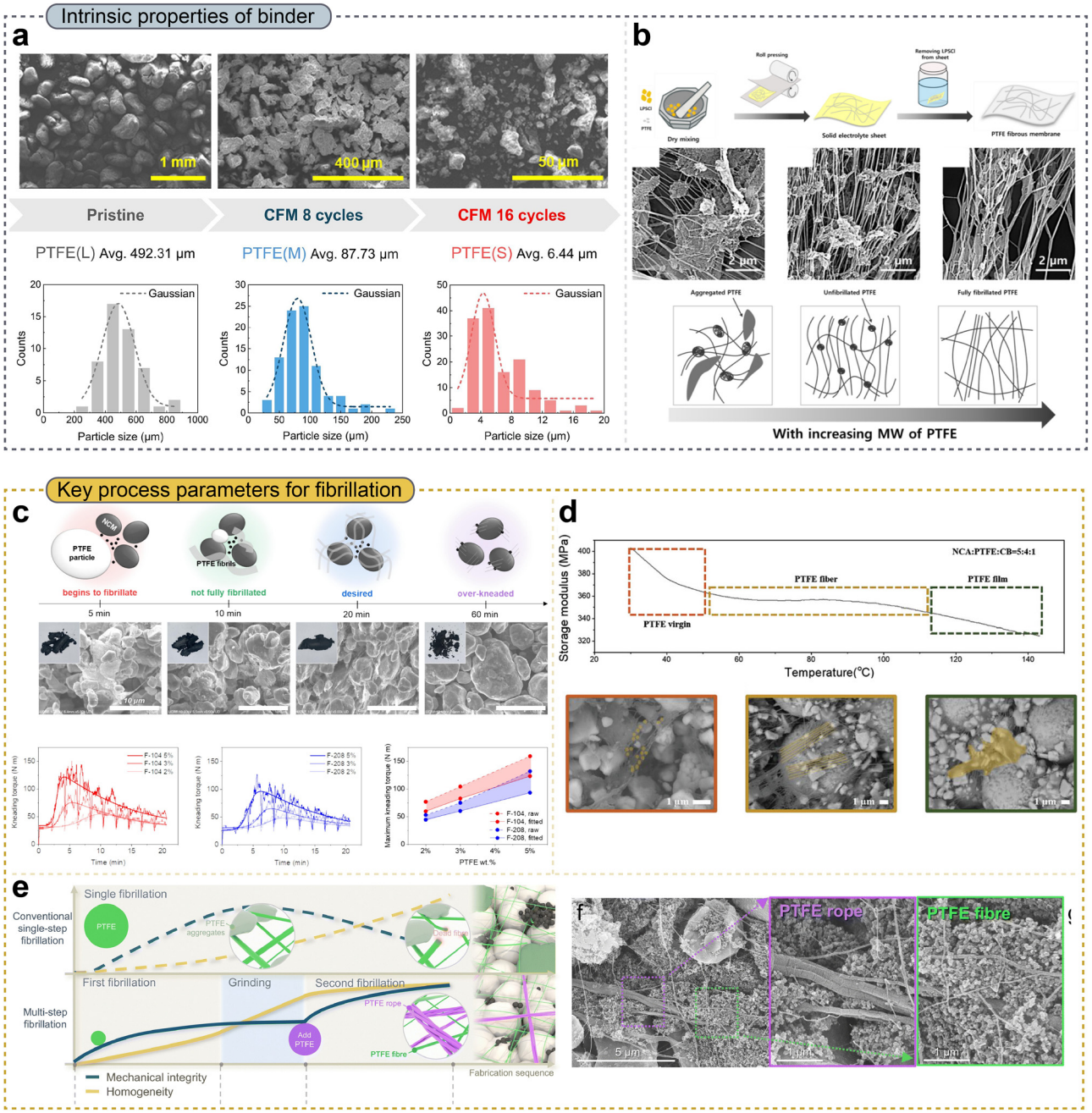

Fig. 4 (a) SEM images (top) and particle size distribution (bottom) of cryo-pulverized PTFE powders. Reproduced with permission from ref. 76. Copyright 2024, Elsevier B.V. (b) Processing schematic of the solid electrolyte sheet formation (top). SEM image (middle) and a predictive fibrillation model for different molecular weights (bottom). Reproduced with permission from ref. 85. Copyright 2024, Elsevier B.V. (c) Schematic illustration of the morphological changes of the PTFE binder with kneading time (top), corresponding SEM images (middle), and kneading torque profiles (bottom). Reproduced with permission from ref. 55. Copyright 2024, Elsevier B.V. (d) Storage modulus of PTFE at different temperatures (top) and corresponding SEM images (bottom). Reproduced with permission from ref. 77. Copyright 2024, Wiley-VCH GmbH. (e) Schematic illustration of the multi-step fibrillation process (left) and SEM images of rope- and fiber-like PTFE morphologies at different feeding times (right). Reproduced with permission from ref. 88. Copyright 2025, The Royal Society of Chemistry.

fibrillation occurred, resulting in PTFE remaining largely in a virgin-like morphology and exhibiting a low tensile strength of 0.43 MPa. In contrast, kneading at 80 °C led to a well-developed, fully fibrous PTFE morphology, accompanied by a significant increase in tensile strength to approximately 0.85 MPa. When the kneading temperature was increased to 135 °C, which exceeds the glass transition temperature (T_g) of PTFE, the fibrils tended to coalesce into film-like structures, indicating excessive softening. Notably, fibrillation at an optimized temperature of 80 °C resulted in a more homogeneous distribution of PTFE and conductive additives, thereby facilitating continuous ion and electron transport pathways, which, in

turn, reduced the ionic resistance (R_{ion}) and charge transfer resistance (R_{ct}). Lee *et al.*[87] comprehensively investigated the effects of PTFE processing on tensile stress and ionic conductivity during the fabrication of solid electrolyte sheets. As the number of calendering loops increased, the tensile stress increased, whereas the ionic conductivity remained at comparable levels. Furthermore, similar tensile stresses were observed at uniaxial (perpendicular to the fibrillation direction) and biaxial fibrillation directions. However, when the uniaxial fibrillation was aligned parallel to the fibrillation direction, a lower tensile strength was attained. This degradation was attributed to the aggregation of 1D PTFE fibers. In contrast, biaxial fibrillation resulted in a random distribution of fibers, leading to an improved tensile strength. As an alternative strategy for achieving uniform fibrillation, Lee *et al.*[88] introduced a dual-fibrous DPE fabrication method in which multistep kneading and grinding were performed as shown in Fig. 4e. This multistep grinding–kneading process enabled the uniform distribution of two types of PTFE fibers—yarn-like thin fibers and rope-like thick fibers—resulting in homogeneous microstructures at both the macroscopic and microscopic scales and leading to an enhanced electrochemical performance. The rope-like fibers improved the mechanical strength by reducing the edge roughness and enhancing the cohesion and adhesion within the electrode.

In summary, the selection of intrinsic material properties of the PTFE binder, together with the fibrillation processing conditions, governs the mechanical integrity and the ionic and electronic pathways of electrodes. Therefore, beyond carefully selecting PTFE binder properties, the optimization of fibrillation processes is essential for scalable DPE fabrication.

3.3. Laminating process

The laminating process provides sufficient adhesion between an electrode layer and a metallic current collector, thereby ensuring the mechanical integrity of the electrode. However, in PTFE-based DPEs, the bonding strength with metallic current collectors is limited; instead, interfacial adhesion is dominated by limited mechanical interlocking.[89–91] In addition, PTFE exhibits a low surface energy of approximately 18 mN m^{-1}, whereas aluminum (Al) current collectors have significantly higher surface energies of approximately 40 mN m^{-1}.[91,92] This noticeable difference in surface energy leads to a reduced work of adhesion at the electrode–current collector interface, further worsening the interfacial adhesion strength.[93–95] Moreover, the interfacial adhesion between the electrode and the current collector is characterized by localized point-to-point contact, as PTFE provides binding through fibrillation. The effective contact area is severely limited, leading to inherently low interfacial adhesion strength. Addressing the weak interfacial adhesion, therefore, necessitates the development of advanced current collector designs and surface modification strategies.

3.3.1. Current collectors. Current collectors in WPEs have been extensively studied to enhance their wettability toward electrode slurries and binders, enhance tensile strength, increase corrosion resistance, and reduce contact resistance.[16,96–99] However, despite their critical role, the function and design of current collectors in DPEs have received comparatively limited attention. Wang *et al.*[100] systematically investigated three different types of current collectors and evaluated their effects on electronic conductivity and interfacial adhesion (Fig. 5a). They found that higher interfacial adhesion led to improved electronic conductivity, and this conductivity varied depending on the type of current collector. Traditional Al current collectors (TACCs), which have a relatively smooth surface, exhibit weak interfacial adhesion. In contrast, etched Al current collectors (EACCs) feature a honeycomb-like structure with submicron-sized pores that can accommodate active materials, resulting in moderately enhanced adhesion. Porous-carbon-coated Al current collectors (PACCs) not only exhibit high electronic conductivity but also provide strong interfacial adhesion. A 180° peel test revealed a pronounced dependence of interfacial adhesion on the type of current collector. The TACC exhibited a low peel strength of approximately 0.28 N, whereas the EACC showed a moderate value of ~6.88 N, and the PACC achieved the highest peel strength (25.42 N). This phenomenon was attributed to the roughness of the surface structures, which effectively increased the interfacial contact area. The enhanced interfacial adhesion led to improved electronic conductivity, with the PACC exhibiting higher conductivity (0.83 S m^{-1}) compared to the TACC (0.25 S m^{-1}). Furthermore, galvanostatic intermittent titration technique (GITT) analysis revealed that the lithium-ion diffusion coefficients of the EACC and TACC were 9.91×10^{-8} and 8.84×10^{-8} cm^2 s^{-1}, respectively, whereas the PACC displayed a significantly higher diffusion coefficient of 1.36×10^{-7} cm^2 s^{-1}. Overall, the PACC demonstrated superior electrochemical performance, highlighting that strong interfacial adhesion facilitates the formation of homogeneous electron transport pathways, which play a critical role in governing electrochemical behavior. However, such coatings typically increase the fraction of electrochemically inactive components, leading to a reduction in energy density. As an alternative strategy for modifying Al current collectors, Kim *et al.*[101] reported an approach in which Al is anodized to form an Al_2O_3 nanotube array, followed by the removal of the top layer to create a nano-embossed porous surface (Fig. 5b). X-ray photoelectron spectroscopy (XPS) analysis revealed that the nanostructured Al current collector (NSA) exhibited metallic Al peaks comparable to those of pristine Al, indicating the successful removal of the Al_2O_3 layer *via* chemical etching. Consequently, the NSA preserved the chemical bonding structure of pure Al, leading to enhanced charge transfer owing to the absence of Al_2O_3, which has high resistivity. Furthermore, a 180° peel test demonstrated that the NSA achieved a peel strength of 1.44 N cm^{-1}, significantly exceeding that of bare Al (0.30 N cm^{-1}), because of mechanical interlocking induced by the nanostructured surface. To quantitatively analyze interfacial interactions, force–distance spectroscopy was performed using atomic force microscopy (AFM). The unbinding force increased from 3.06×10^{-9} N for

bare Al to 6.79×10^{-9} N for the NSA, while the adhesion energy increased from 2.18×10^{-17} to 8.21×10^{-17} J. Therefore, the electrochemical evaluations demonstrated superior rate capability and overall electrochemical performance.

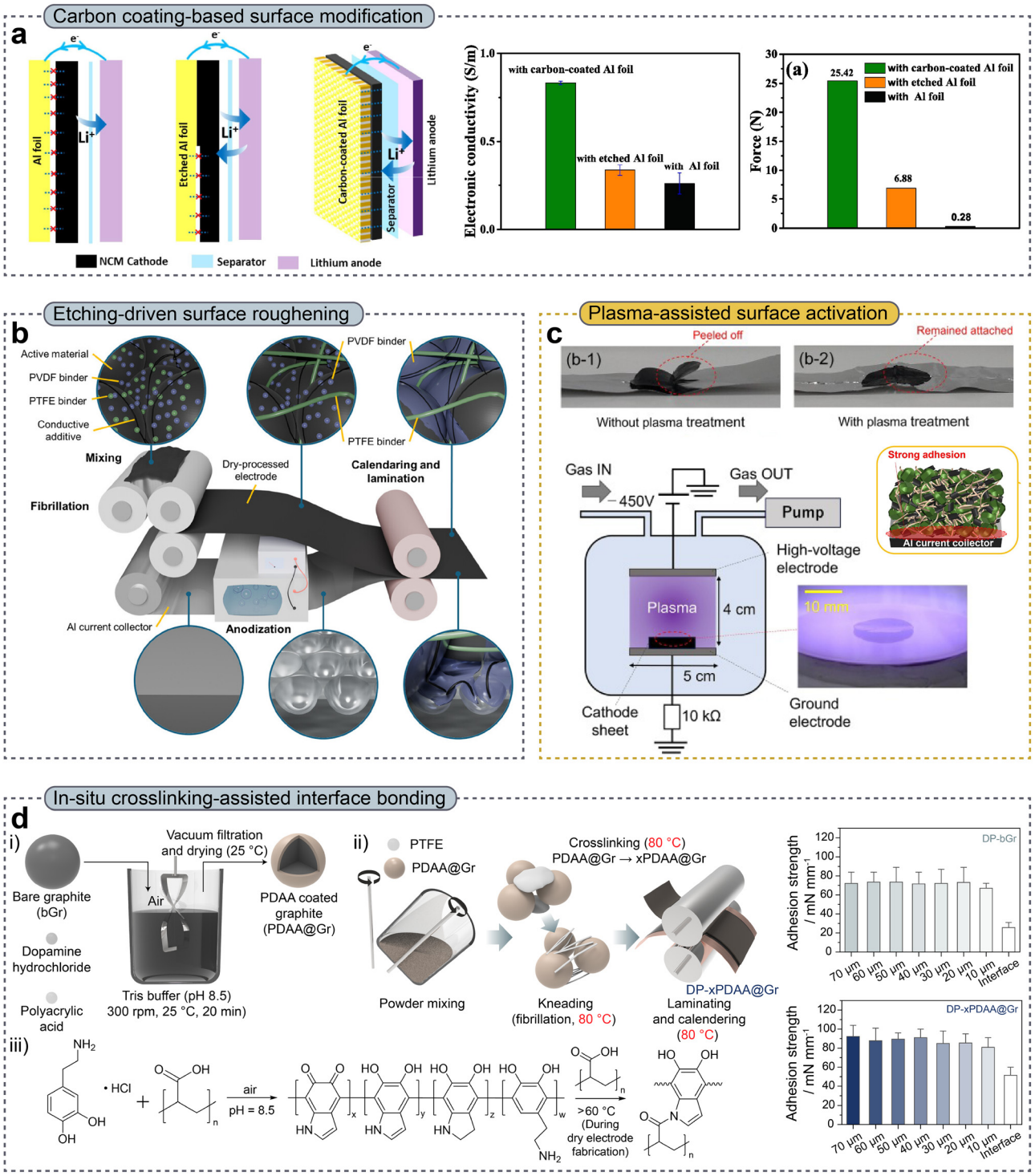

Fig. 5 (a) Schematic illustration of electrodes fabricated on various current collectors (left), electronic conductivity (middle), and adhesion force (right). Reproduced with permission from ref. 100. Copyright 2024, Elsevier B.V. (b) Anodization process applied to aluminium current collectors to induce surface roughness. Reproduced with permission from ref. 101. Copyright 2025, Wiley-VCH GmbH. (c) Photographic images of the current collectors with and without plasma treatment (top). Schematic illustration of plasma treatment for surface activation (bottom). Reproduced with permission from ref. 108. Copyright 2025, Elsevier B.V. (d) Schematic illustration of crosslinking-assisted polymer interfacial bonding to reinforce the mechanical robustness of the electrode (left). Adhesion strength of DP-bGr and DP-xPDAA@Gr (right). Reproduced with permission from ref. 15. Copyright 2025, Wiley-VCH GmbH.

3.3.2. Surface modification. The surface modification of binders has been widely employed to enhance interfacial adhesion.[102–104] Plasma treatment is a well-recognized dry surface modification process and has been reported to effectively improve interfacial adhesion through surface functionalization.[105–107] As shown in Fig. 5c, Kanno *et al.*[108] applied plasma treatment to the top surface of DPEs, introducing hydroxyl (–OH) groups onto the PTFE surface and, thereby, converting the inherently nonpolar PTFE into a more polar material, which enhanced the interfacial adhesion. During plasma treatment, the crystal structures of cathode active materials such as LFP and NCM remained largely unchanged, and PTFE was confirmed to be selectively functionalized. The plasma-treated electrodes exhibited significantly enhanced interfacial adhesion, along with improved electrochemical performance. Moreover, our group reported that graphite particles coated with polydopamine (PD) and PAA induced *in situ* chemical crosslinking during a dry fabrication process conducted at 80 °C (Fig. 5d).[15] The amine groups ($-NH_2$) of PD and the carboxylic acid groups (–COOH) of PAA formed robust amide (–RNCO–) bonds, which occurred within the composite layer and between adjacent coating layers, resulting in the formation of a highly interconnected 3D network. XPS analysis revealed that PD-coated graphite (PD@Gr) showed characteristic $-NH_2$ and –HN–R peaks, whereas graphite particles coated with both PD and PAA (PDAA@Gr) showed an additional amide (–RNCO–) peak. SAICAS analysis was performed to further elucidate the role of amide bonding. Compared with pristine dry-processed Gr (DP-bGr), DP-PD@Gr and DP-xPDAA@Gr exhibited higher interfacial adhesion and enhanced adhesion strength within the electrode. These results indicate that, during DPE fabrication, *in situ* crosslinking effectively enhances the overall mechanical robustness of the DPE. Electrochemical evaluations showed that, after 500 cycles, DP-xPDAA@Gr and DP-PD@Gr showed values of 87.1% and 84%, respectively, whereas DP-bGr exhibited a lower capacity retention of 77.9%.

The lamination process is a critical step for enhancing the interfacial adhesion between an electrode and a current collector, as the adhesion at the electrode–current collector interface directly influences electronic conductivity and contact resistance, ultimately dictating electrochemical performance. Although carbon coating, etching, plasma treatment, and crosslinking-assisted polymer bonding strategies have improved interfacial adhesion, from a processing perspective, carbon-coated Al current collectors still require systematic investigation to identify suitable conductive additives and binders, optimize the coating thickness, and determine the optimal fraction of carbon-coated Al within the electrode architecture. Moreover, the Al etching process requires optimization to fully exploit its potential in enhancing interfacial adhesion and electronic transport pathways.

3.4. Calendering process

Calendering has long been recognized as a critical post-fabrication step that strongly influences the mechanical integrity and electrochemical performance of battery electrodes. This process is believed to play a multifunctional role by simultaneously determining electrode density, particle–particle contact, adhesion to the current collector, and electronic and ionic transport properties.[39,109,110] Beyond porosity reduction, calendering in DPEs performs an additional and essential function by continuing the fibrillation of polymeric binders such as PTFE. Rolling and pressing introduce substantial shear stresses that further extend, align, and redistribute the PTFE fibrils throughout the electrode thickness. This shear-induced fibrillation reinforces the mechanically interlocking binder network that connects active material particles and conductive additives, enhancing electrode cohesion and stabilizing particle–particle contact.[32,111–113]

3.4.1. Densification. Effective densification during calendering contributes to an increased electrode density, thereby improving the electronic connectivity and reducing contact resistance within electrodes. Fig. 6a schematically illustrates DPE calendering and highlights the distinct mechanical regimes governing electrode formation, namely the feed zone and the nip zone. In the feed zone, powder transport into the roll gap is dominated by frictional forces between particles and the roll surfaces, along with internal particle–particle friction, which collectively generate pronounced shear planes approximately parallel to the roll surface. These shear fields redistribute conductive additives and polymeric binders, further promoting binder fibrillation. As the powder progresses into the nip zone, the shear gradually diminishes and normal compressive stress increases sharply, leading to densification and consolidation of the electrode film. Importantly, Gyulai *et al.*[112] demonstrated that effective DPE formation relies on maximizing the shear-dominated feed zone while minimizing excessive compaction in the nip zone, in contrast to conventional wet-process calendering where shear is typically avoided. This shear-dominant calendering ensures a homogeneous redistribution of the binder, continuous fibril formation, and uniform density profiles across the electrode thickness, thus directly linking calender design and operating parameters to densification quality, mechanical cohesion, and electrochemical performance. Despite these advantages, the densification behavior during DPE calendering is highly sensitive to the intrinsic mechanical properties of the binder system. For instance, when PTFE alone is used as the binder, multiple calendering passes are often required to reach the target electrode thickness, reflecting the high stiffness and limited plastic deformability of PTFE under compressive stress. To overcome these limitations, PTFE composite binders incorporating non-fibrillizable polymers such as PVdF or PEO can be co-introduced. These secondary binders provide enhanced ductility and flowability during calendering, enabling efficient thickness reduction with significantly fewer roll passes, while also preserving the mechanical cohesion of the electrode.[114]

Along with binder properties, the architecture of active materials also greatly determines the densification behavior during calendering.[37,115–118] Hong *et al.*[116] systematically demonstrated that bimodal particle-size distributions

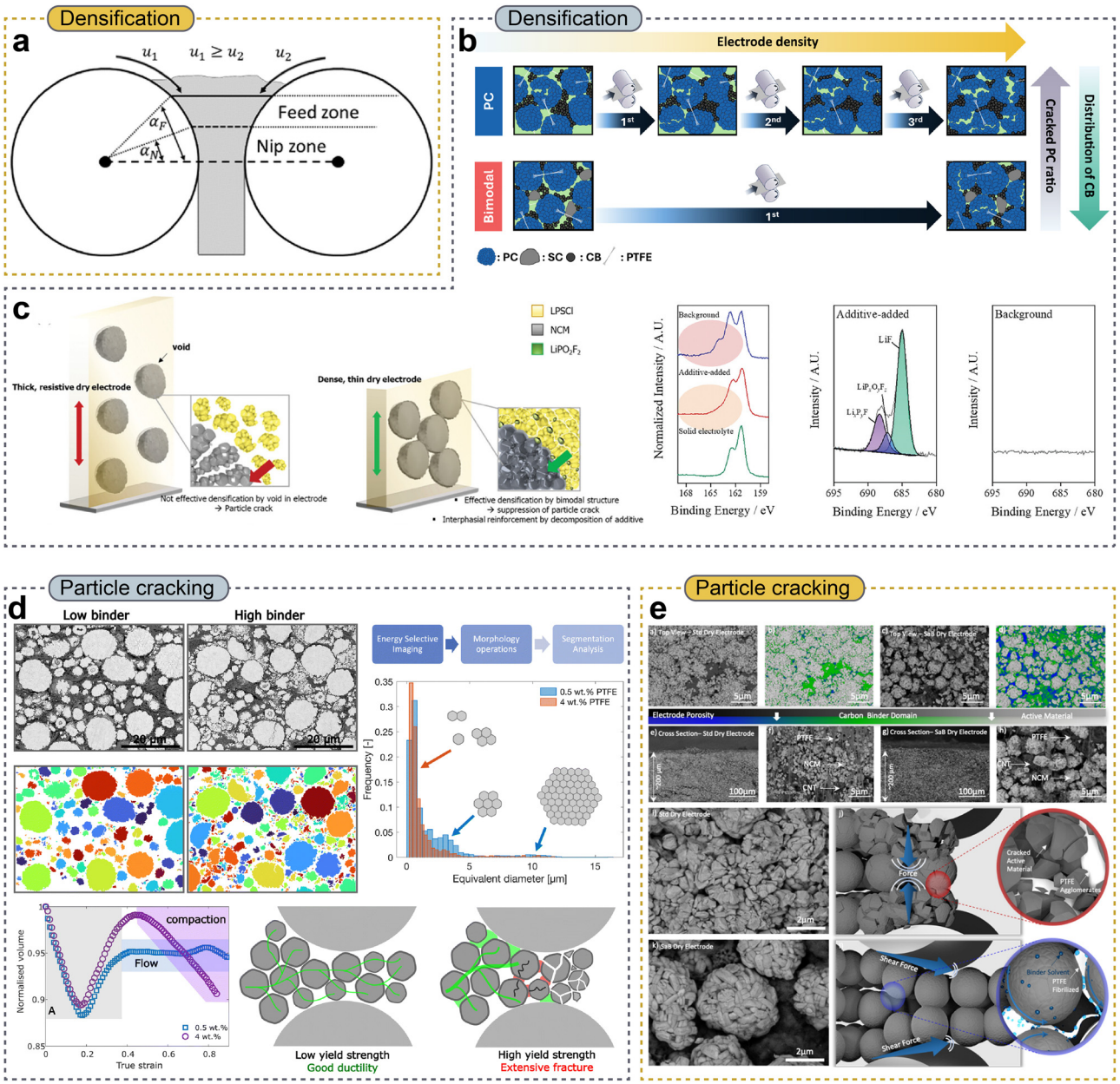

Fig. 6 (a) Scheme of a vertical powder calendering process with the distinct gap zones and characteristic parameters. Reproduced with permission from ref. 112. Copyright 2023, American Chemical Society. (b) Schematic illustration of comparison of overall characteristics between PC and bimodal electrodes. Reproduced with permission from ref. 116. Copyright 2025, Elsevier B.V. (c) Scheme of the distinguished ability of $LiPO_2F_2$ as an electrode additive, and S 2p and F 1s XPS spectra of background and $LiPO_2F_2$-added electrodes after the formation in all-solid-state batteries. Reproduced with permission from ref. 119. Copyright 2023, Wiley-VCH GmbH. (d) Energy-selective backscattered electron micrographs and segmented images of NCM particles for electrodes with low (0.5 wt%) and high (4 wt%) PTFE binder contents (left), corresponding NCM particle size distributions (right), and normalized volume evolution under uniaxial compression with schematic illustrations of deformation behavior during calendering (bottom). Reproduced with permission from ref. 122. Copyright 2025, The Royal Society of Chemistry. (e) SEM images of standard DPEs and solvent-assisted binder (SaB) DPEs, including surface and cross-sectional morphologies (top) and high-magnification cross-sectional views with schematics illustrating microstructural evolution during calendering (bottom). Reproduced with permission from ref. 123. Copyright 2024, Elsevier B.V.

combining large polycrystalline (PC) and small single-crystalline (SC) particles enhanced packing density by efficiently filling interstitial voids, thereby reducing the number of calendering passes required to reach the target electrode density (Fig. 6b). Importantly, this densification proceeded through geometric rearrangement rather than particle fracture, resulting in a lower fraction of mechanically damaged particles compared to that of unimodal PC electrodes at comparable densities. Furthermore, the higher intrinsic packing density of bimodal electrodes suppressed elastic spring-back during electrochemical cycling, preserving particle–particle contact and electronic percolation networks. These effects collectively lead

to improved electronic stability and cycling performance, underscoring the fact that effective densification in calendering arises from the coupled interactions between shear-induced binder fibrillation and particle-scale packing, rather than from compressive stress alone. Similarly, Kim *et al.*[119] have provided direct evidence that conventional DPE preparation intrinsically exhibits incomplete and spatially non-uniform densification during calendering, contributing to persistent microstructural defects such as interparticle voids and particle cracking after rolling (Fig. 6c). In their study, voids were widely spread throughout the mixed powder before calendering, leading to a sparse bulk structure in the as-pressed electrode because the externally applied pressure was not evenly transmitted through the heterogeneous powder bed. Consequently, regions with residual voids exhibited poor mechanical load transfer during calendering. This resulted in persistent porosity as well as the development of microcracks within active materials and at interfacial points of contact. To mitigate these chemo-mechanical shortcomings, a bi-functionalized electrode additive approach was introduced, in which a finely dispersed electrolyte component (Li_6PS_5Cl) and a lithium difluorophosphate ($LiPO_2F_2$) additive were incorporated into the electrode mixture. The bimodal particle size distribution and strategic filling of interparticle voids by the additive facilitated a more uniform pressure distribution under calendering, enhancing powder packing and reducing residual voids and cracking. Additionally, the $LiPO_2F_2$ additive readily reacted with the surfaces of the active material during initial electrochemical formation, producing a conformal LiF/Li_xPF_y surface layer, which further improved the chemo-mechanical stability and suppressed solid electrolyte degradation. These findings collectively underscore that achieving homogeneous densification during calendering is a prerequisite for suppressing void formation, ensuring uniform stress transfer, and maintaining the mechanical and electrochemical integrity of DPEs.

3.4.2. Particle cracking. As discussed previously, particle cracking represents a critical calendering-induced degradation, fundamentally distinct from electrochemically driven fracture during cycling.[39,120,121] Unlike WPEs, which typically contain a continuous polymeric binder formed during slurry drying, DPEs are consolidated through direct solid–solid interactions among active material particles, conductive additives, and fibrillated PTFE networks. Matthews *et al.*[122] reported that stress accommodation during calendering was governed primarily by the viscoelastic response and structural continuity of the PTFE binder network. In addition, PTFE-based DPEs exhibit a characteristic viscoelastic deformation behavior comprising three regimes: an initial elastic response, followed by a ductile flow region associated with PTFE fibril deformation, and finally a high-stress compaction regime in which particle rearrangement becomes constrained and stress is transferred directly to active material particles (Fig. 6d). Once an electrode enters this compaction-dominated regime, local stress concentrations develop at particle–particle contacts and within densely packed clusters, providing a mechanical driving force for particle fracture. Calendering-induced particle cracking has been shown to depend greatly on the binder fraction and its resulting influence on the electrode stiffness and yield strength. Increasing the PTFE content beyond a certain threshold results in a non-linear increase in both the Young's modulus and yield stress of the electrode composite, thereby reducing its ability to undergo plastic deformation during compression. Consequently, electrodes with higher binder contents demonstrate extensive fractures of polycrystalline secondary particles during calendering, with cracks propagating preferentially along grain boundaries. Importantly, a study recently showed that such calendering-induced particle cracking is not an inevitable outcome of dry processing but can be substantially mitigated by modifying the calendering pathway. Embleton *et al.*[123] systematically showed that introducing a trace amount of a low-boiling, non-toxic solvent (ethanol, <3 wt%) into a PTFE binder system—referred to as a solvent-assisted binder (SaB) dry process—fundamentally altered stress transmission during calendering (Fig. 6e). Ethanol improved the initial dispersion of PTFE and conductive additives and acted as a transient lubricant during rolling, effectively redistributing externally applied compressive stresses into shear-dominated deformation modes. As a result, PTFE fibrillation was promoted more uniformly, while excessive local stress concentrations at particle–particle contact points were suppressed. Cross-sectional SEM images revealed that, unlike standard DPEs that exhibit pervasive secondary particle cracking throughout the electrode thickness, SaB-processed DPEs largely preserved the spherical morphology of polycrystalline NCM622 particles, even under high mass loading conditions.

In summary, calendering is a critical step in DPE manufacturing and governs electrode densification, binder fibrillation, and mechanical integrity. Effective calendering in DPEs relies on shear-dominated deformation to promote uniform PTFE fibrillation and particle packing. Densification is strongly influenced by binder mechanics and particle architecture, while inadequate stress accommodation leads to non-uniform consolidation and calendering-induced particle cracking. Importantly, particle fracture is not intrinsic to dry processing but can be mitigated by controlling materials design and calendering pathways, allowing for mechanically robust and high-performance DPEs.

4. Advanced binders for next-generation dry-processed electrodes

4.1. Challenges in conventional PTFE binders

PTFE has become one of the most widely adopted binders for DPE owing to its exceptional and unique fibrillation behavior under shear.[32,117,124] However, conventional PTFE binders present several fundamental challenges that limit their broader applicability (Fig. 7a). A major challenge is the inherently non-uniform dispersion of PTFE within composite electrodes. In DPE fabrication, binder dispersion is governed primarily by mechanical mixing and shear-driven fibrillation, rather than by solvent-mediated molecular diffusion. Under such conditions,

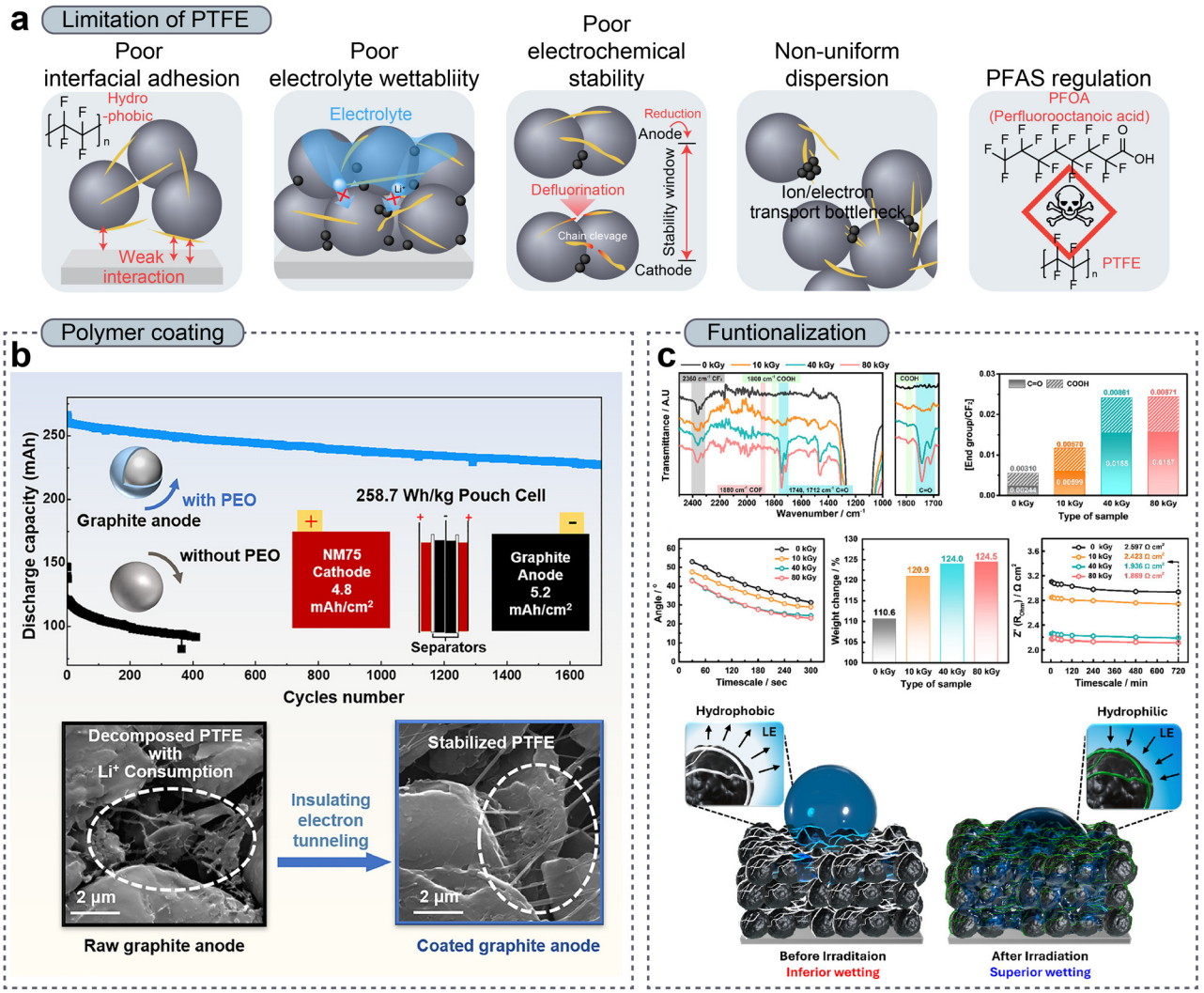

Fig. 7 (a) Schematic illustration of challenges in the PTFE binder in DPEs. (b) Prevention of PTFE decomposition through PEO coating on a graphite anode. Reproduced with permission from ref. 129. Copyright 2024, Cell Press. (c) FT-IR spectra, molar ratio of the oxygen group, contact angle, weight change of the electrodes after being soaked for 1 h, and R_{ohm} resistance of the electrodes over time as a function of irradiation dose (top) and schematic of electron beam-induced functionalization of fibrillated PTFE in post-fabricated dry electrodes (bottom). Reproduced with permission from ref. 134. Copyright 2025, Wiley-VCH GmbH.

PTFE particles do not always undergo uniform fibrillation throughout the electrode. Instead, localized PTFE agglomerates or uneven fibrillar clusters frequently form, resulting in spatial heterogeneity in binder distribution.[57,88,125,126] This non-uniform binder network can induce localized ionic and electronic transport bottlenecks, particularly in regions where excessive PTFE aggregation disrupts continuous conductive pathways or blocks pore channels. Consequently, such structural heterogeneity compromises electrochemical performance by increasing local resistance and limiting the effectiveness of utilizing active materials.

Furthermore, under low potential, PTFE may be susceptible to reductive decomposition owing to the low lower unoccupied molecular orbital (LUMO) level. When using PTFE as an anode binder, the defluorination of PTFE results in a lower initial coulombic efficiency (ICE) and chain cleavage, which degrade mechanical robustness. To address this, electrolyte additives such as FEC (fluoroethylene carbonate) can be used to form a proactive and stable FEC-derived solid electrolyte interphase (SEI)[127,128] and polymer coating on active materials, providing an option for suppressing irreversible PTFE reactions.[129,130] As shown in Fig. 7b, Z. Wei *et al.*[129] systematically elucidated the electrochemical reduction and defluorination of PTFE binders in dry-processed graphite anodes and found that a thin PEO coating on graphite particles effectively suppressed PTFE decomposition by electronically decoupling the binder from the anode while maintaining lithium-ion transport, thereby enabling the development of high-loading DPEs with significantly improved ICE and practical pouch-cell performance.

Another critical limitation of PTFE binders is found in their poor interfacial adhesion to active materials and current collectors. As mentioned in the Laminating process section, the

chemically inert and nonpolar nature of PTFE composed of C–F bonds results in weak interfacial interactions with metallic current collectors, where adhesion relies mainly on mechanical interlocking rather than on chemical bonding.[89,90,131] In DPEs, where the binder content is typically minimized, insufficient interfacial adhesion can lead to delamination at the electrode–current collector interface and reduced mechanical robustness under calendering or cycling-induced stress. This issue becomes particularly problematic in thick, high-loading electrodes, where insufficient interfacial contact not only undermines structural integrity but also increases interfacial contact resistance, thereby limiting effective electronic transport across the electrode thickness. As electrode thickness increases, such interfacial electronic bottlenecks can promote non-uniform current distribution and depth-dependent electrochemical utilization, underscoring the need to address adhesion and interfacial design as critical factors in fabricating thick DPEs.

Beyond adhesion-related concerns, facile electrolyte penetration becomes increasingly critical in thick DPE configurations, where lithium-ion transport must be sustained across through-thickness pathways. While fibrillated PTFE networks can form open-channel microstructures that are more favorable for ion transport compared to conventional WPEs,[132–135] the intrinsically low electrolyte affinity of PTFE remains a key limitation. In DPEs, where the porosity and tortuosity are carefully controlled through calendering, poor electrolyte wettability can cancel the benefits of optimized densification by limiting the effectiveness of ionic transport. Moreover, delayed or incomplete wetting can result in increased interfacial resistance, a non-uniform current distribution, and sluggish electrochemical activation. These effects are exacerbated in thick electrodes, where electrolyte penetration is already kinetically constrained. To address this, Won *et al.*[151] proposed a post-fabrication functionalization strategy where fibrillated PTFE binders within DPEs are selectively modified *via* electron-beam (EB) irradiation to introduce oxygen-containing functional groups such as –COOH and C═O. This can effectively convert intrinsically hydrophobic PTFE surfaces into electrolyte-affinitive interfaces without compromising fibrillation behavior or mechanical integrity (Fig. 7c). As a result, the EB-treated DPEs exhibited markedly improved electrolyte wettability, enhanced electrolyte uptake, and significantly reduced ionic transport resistance throughout the entire electrode thickness. Importantly, this improvement has enabled uniform lithium-ion migration even in hyper-thick electrodes with mass loadings up to 100 mg cm^{-2}, thereby mitigating through-thickness reaction inhomogeneity and suppressing localized overpotential accumulation. Similarly, Kanno *et al.*[108] used a plasma-assisted dry process to introduce oxygen-containing functional groups (–OH) onto PTFE surfaces. By simply applying plasma treatment to a cathode sheet composed of PTFE, an active material, and a conductive additive, the electrolyte wettability and adhesion were improved, resulting in an enhanced electrochemical performance compared with that of a non-treated cathode. These findings clearly demonstrate that the surface modification of PTFE binders represents a critical design strategy for overcoming the electrolyte wetting limitations of DPEs, particularly under high mass loading conditions.

Apart from performance-related concerns, environmental recycling and health-related challenges associated with PTFE are becoming increasingly imporant.[136–140] PTFE is classified within the broader family of per- and polyfluoroalkyl substances (PFASs), a class of fluorinated compounds which are under increasing regulatory scrutiny due to their extreme environmental persistence, potential for bioaccumulation, and emerging links to human health hazards. Owing to its strong chemical and thermal stability, PTFE is often associated with the ''forever chemical'' concern, as degradation in the environment is slow and end-of-life handling is difficult.[161,162] While this stability is advantageous for electrode integrity, it also creates challenges from a lifecycle perspective, particularly for waste treatment and recycling of PTFE-containing electrodes. As a result, persistent fluorinated components may increase cumulative environmental burden and limit efficient material recovery through recycling routes.[163,164] In particular, increasing attention has been directed toward perfluorooctanoic acid (PFOA) and related long-chain PFAS, which were historically used as processing aids or surfactants during PTFE polymerization. Although PFOA is not intentionally present in the final PTFE product, residual traces and lifecycle-related considerations, including emissions during manufacturing and impacts during disposal, have led regulators to evaluate PTFE-containing materials within the broader PFAS framework. In summary, the challenges associated with non-uniform dispersion, interfacial instability, limited electrolyte wettability, electrochemical instability at low electrode potentials, and growing environmental, recycling, and health considerations under PFAS-related regulation support the need to move beyond conventional PTFE binders toward more sustainable material systems for DPEs.

4.2. Dual-binder and beyond-PTFE binder (PFAS-free) systems

While substantial efforts have been made to address the limitations of PTFE-based DPEs through process optimization and interfacial engineering, growing evidence suggests that many of these challenges are intrinsically linked to the fundamental physicochemical nature of PTFE. Consequently, research interest has been directed toward dual-binder strategies and beyond-PTFE, PFAS-free binder systems that provide both mechanical robustness and enhanced electrochemical functionality. Dual-binder systems are effective systems in which PTFE is combined with a secondary polymer binder, *i.e.*, a co-binder. In this approach, PTFE primarily serves as a mechanically robust, fibrillating scaffold that enables solvent-free electrode fabrication, while the co-binder introduces other functionalities. Many of the co-binders employed in dual-binder DPE systems, including PVdF and hydrophilic polymers such as PAA, carboxymethyl cellulose (CMC), and PVP, have been extensively investigated in WPEs and are generally regarded as chemically and electrochemically stable within the practical operating voltage window of LIBs.[165–168] Sung *et al.*[90] demonstrated a representative dual-binder strategy that

integrates PAA as a hydrogen-bonding co-binder into PTFE-based DPEs. By partially replacing PTFE with PAA while maintaining a low total binder content, a substantial enhancement in adhesion between the freestanding electrode film and the Al current collector was achieved, attributed to hydrogen bonding between the carboxyl groups (–COOH) of PAA and hydroxyl groups (–OH) present on the native Al_2O_3 layer on the Al current collector (Fig. 8a). This chemical adhesion mechanism stood in sharp contrast to the purely mechanical anchoring provided by PTFE fibrils alone and effectively mitigated interfacial delamination under both calendering-induced stress and long-term electrochemical cycling. Beyond adhesion, the introduction of PAA significantly improved the electrolyte wettability by increasing the surface energy of the electrode and promoting favorable interactions with polar carbonate-based electrolytes. Contact angle measurements and impedance analyses clearly confirm accelerated electrolyte infiltration, reduced interfacial resistance, and enhanced lithium-ion transport throughout the electrode thickness, particularly under high mass loading conditions. Importantly, these interfacial improvements were achieved without compromising the PTFE fibrillation behavior or mechanical integrity, enabling stable electrochemical performance in thick, high-density DPEs. Similarly, He *et al.*[141] introduced a biomass-derived flour additive at low loading (1 wt%) into PTFE-based DPEs to form flour-infused DPEs with enhanced structural and transport properties. The crosslinking between protein and starch components in the flour, in combination with PTFE fibrillation, resulted in the formation of a highly flexible and mechanically resilient powder network with robust load transfer during calendering. Importantly, the modified microstructure exhibited a larger, more interconnected pore architecture that reduced the pore tortuosity in the electrode, thereby improving the ion transport kinetics compared with those of conventional PTFE-only DPEs. DPEs incorporating 1 wt% flour demonstrated superior mechanical integrity and enhanced rate capability and cycling stability, along with the suppressed irreversible phase transitions and intragranular/intergranular crack propagation under aggressive cycling conditions. These findings show that hybrid additive approaches, in which low-cost and sustainable powders are integrated into PTFE fibrillated matrices, can effectively address major bottlenecks in DPE performance by simultaneously reinforcing mechanical cohesion and ion transport behavior. Along with strategies that target interfacial adhesion and wettability, recent efforts have focused on enhancing the electrochemical stability of PTFE-based DPEs by integrating functional co-binders that stabilize the active material–binder interface under reductive conditions.[142,143] For example, Lee *et al.*[142] reported a dual-binder system consisting of PTFE and PVP for dry-processed graphite anodes, in which PVP effectively reduced direct contact between PTFE and the anode surface, suppressed PTFE decomposition, and facilitated the formation of a robust, inorganic-rich SEI that enhanced the lithium-ion kinetics and interfacial stability (Fig. 8b). Consequently, DPEs using the PVP/PTFE binary binder achieved an ultrahigh areal capacity (10 mAh cm^{-2}) with significantly improved ICE and prolonged cycling stability compared with those of PTFE-only counterparts.

Furthermore, recent studies are increasingly emphasizing the influence of binder dispersion and network uniformity on the mechanical integrity and electrochemical performance of DPEs.[144,145] For instance, Kang *et al.*[145] introduced a bollard-anchored dual-binder architecture in which a PAA-grafted-sodium carboxymethyl cellulose (PAA-*g*-CMC) functioned as a dispersion-controlling "bollard," effectively anchoring PTFE fibrils and suppressing binder agglomeration (Fig. 8c). This architecture effectively suppressed binder agglomeration by immobilizing PTFE fibrils through multivalent hydrogen bonding and polymer–polymer anchoring, thereby preventing uncontrolled fibril bundling and the development of localized binder-rich domains during dry mixing and calendering. As a result, the dual-binder system promoted a more homogeneous binder network throughout the electrode thickness, significantly improved powder dispersion, and enabled uniform stress and charge transport even at high mass loadings (90 mg cm^{-2} and 15.6 mAh cm^{-2}), while simultaneously reducing the overall PTFE content.

Building upon dual-binder strategies that partially alleviate the intrinsic limitations of PTFE, emerging studies are focusing on the development of beyond-PTFE, PFAS-free binder systems that can fundamentally replace fluorinated polymers in DPE manufacturing.[47,60,146–148] In this context, two distinct material design strategies have been explored, namely PFAS-free binders that retain fibrillation behavior under shear and alternative binders that enable dry processing without relying on fibrillation mechanisms. Regarding the former, Schmidt *et al.*[148] reported a renewable, fluorine-free protein-based binder (sericin) that could form fibrillar networks during shear-induced dry processing, similar to PTFE fibrillation. Despite its lower M_W relative to that of PTFE, sericin underwent shear-induced fibril formation, generating a spiderweb-like network that effectively interconnected active materials and conductive additives in solvent-free lithium–sulfur cathodes. Importantly, the intrinsic polarity of the polypeptide binder enhanced the electrolyte wettability and interfacial interactions with polysulfide species, resulting in an electrochemical performance comparable to that of PTFE-based DPEs, even under electrolyte-lean conditions. In addition, this study demonstrated that the fibrillation-enabled mechanical integrity in DPEs is not exclusive to fluoropolymers and can be achieved using biodegradable, PFAS-free macromolecules with appropriate molecular architectures. In contrast, a fundamentally different approach was introduced by Kim *et al.*,[146] who demonstrated fluorine-free DPEs based on a thermoplastic binder (Parafilm® M) that does not rely on fibrillation for mechanical cohesion. Instead, Parafilm, composed of paraffin and polyethylene, exploits its low T_g and thermoplastic flow behavior to establish interparticle bonding through mild pressure activation during dry pressing and calendering (Fig. 8d). This binder enabled primer-free adhesion to current collectors, a uniform binder distribution, and robust mechanical integrity without the formation of fibrillar networks. Notably, the absence of fluorinated moieties

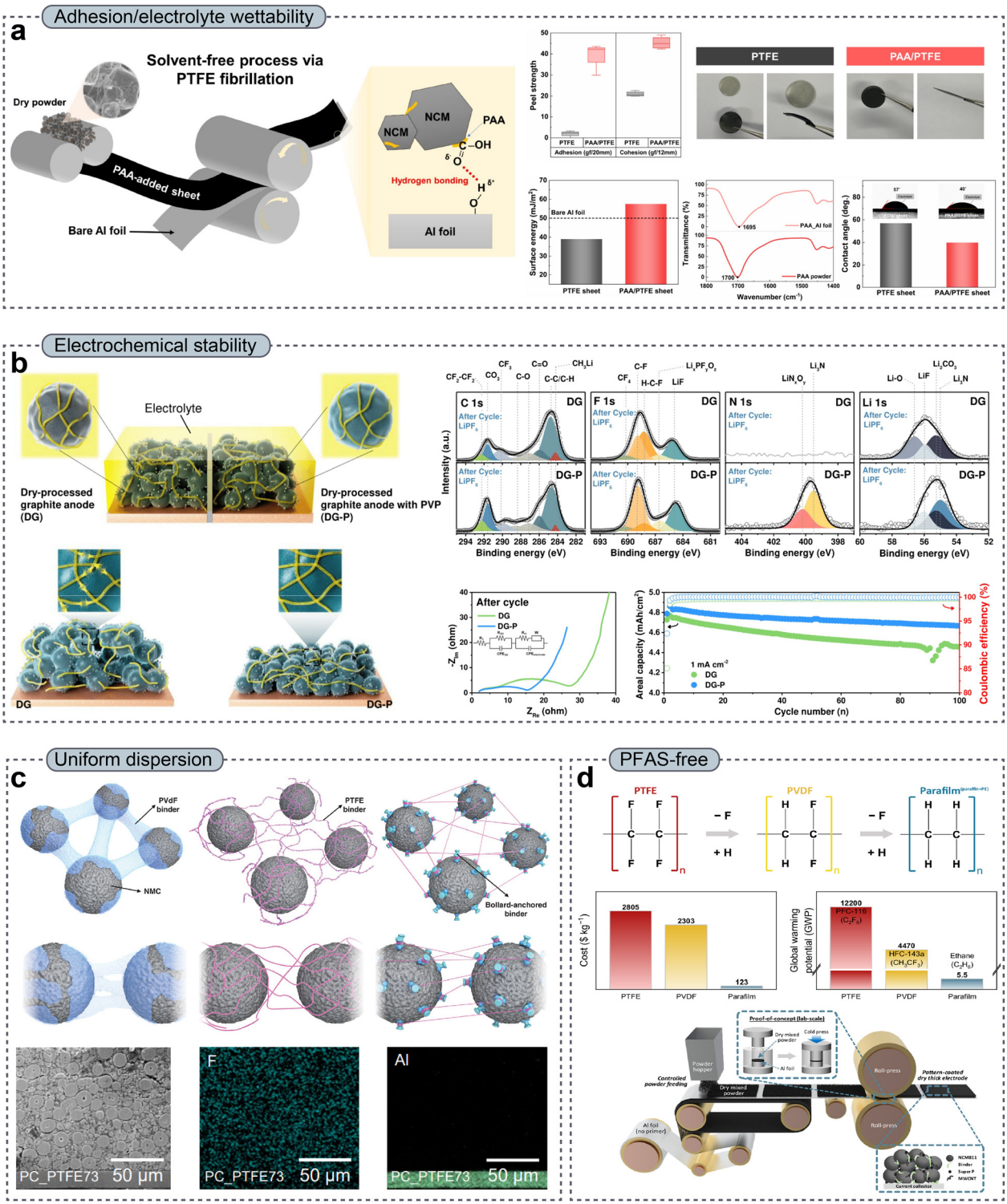

Fig. 8 (a) Schematic illustration of the dry process using a PAA/PTFE dual binder and comparative analysis of adhesion properties of PTFE- and PAA/PTFE-based DPEs, correlated with post-cycling electrode morphologies after 100 cycles, surface energies of Al foil and binder sheets, FT-IR evidence of hydrogen bonding interactions, and contact angle measurements. Reproduced with permission from ref. 90. Copyright 2025, Elsevier B.V. (b) PTFE/PVP dual-binder for mitigating direct contact between PTFE and the anode surface, suppressing PTFE decomposition, and facilitating the formation of a robust, inorganic-rich SEI. Reproduced with permission from ref. 142. Copyright 2025, Wiley-VCH GmbH. (c) Schematic images of a cathode with PVdF (wet process), PTFE (dry process), and bollard-anchored dual-binder (dry process) and cross-sectional SEM/EDS images of a bollard-anchored dual-binder-based cathode. Reproduced with permission from ref. 145. Copyright 2024, Elsevier B.V. (d) Comparison of PTFE, PVDF, and Parafilm binders based on the structure, cost, environmental impact, and manufacturing process. Reproduced with permission from ref. 146. Copyright 2025, Springer Nature.

Table 2 Comparison of dual-binder and beyond PTFE (PFAS-free) binder systems

(a)

Classification		System	Function	Approach	Electrode composition (wt%)			Ref.
					Active material	Conductive additive	Binder	
Dual binder	PTFE/PAA	NCM811 cathode	Improve adhesion and electrolyte wettability *via* polar functional groups of PAA	Twin-screw kneading of the mixed powder	96.8(NCM811)	1.2(carbon black)	2[PTFE/PAA = 1/1(w/w)]	90
	PTFE/High-gluten flour	NCM811, LCO cathode	Improve mechanical robustness *via* flour crosslinking	Hot-pressing of powder mixture	90(LCO/NCM811)	5[Super P/carbon fiber = 4/1(w/w)]	5[PTFE/flour = 4/1(w/w)]	141
	PTFE/PAA-g-CMC	NCM622 cathode	(1) Anchoring PTFE to the electrode surface (2) Improve Li ion transport and adhesion	(1) Pre-anchoring of PAA-g CMC (2) binder onto NCM particles (3) PTFE-assisted fibrillation (4) Kneading and calendering	93(NCM622)	5(Super P)	2[PTFE/PAA-g-CMC = 3/7(w/w)]	145
	PTFE/PVdF	Graphite anode	Functional binder when PTFE decomposes in the first lithiation	(1) PVdF-assisted powder premixing (2) PTFE-induced fibrillation (3) Hot calendering (4) Lamination	90(graphite)	5(carbonblack)	5[PTFE/PVdF = 3/2(w/w)]	149
	PTFE/PVP	Graphite anode	(1) Reducing PTFE decomposition (2) Enhancing mechanical robustness (3) Formation of a robust Li_3N-rich SEI layer	(1) Powder premixing (2) Kneading and calendering (3) Lamination	95.5(graphite)	1(carbon black)	3.5[PTFE/PVP = 6/1(w/w)]	142
	PTFE/CMC	Graphite anode	(1) Reducing PTFE decomposition (2) Improve Li ion transport and adhesion	Quasi-dry processing using ethanol to uniformly integrate CMC	97(graphite)	1(Super P)	2[PTFE/CMC = 1/1(w/w)]	143
PFAS-free	Phenoxy resin	NCM811 cathode	Formation of a continuous and ductile binder network	Hot-pressing a powder composite using a press machine	100(NCM811)	1.5(CNT)	3(phenoxy resin)	150
	Sacrificial binder (PP, paraffin wax, stearic acid)	LFP cathode	Rheological control and structural support during forming, followed by debinding to create a porous, high–active-material electrode	Powder extrusion molding (PEM) technology	—	—	—	60
	Parafilm	NCM811 cathode	(1) Cost effectiveness (2) High electrochemical stability at low potentials (3) Providing natural adhesion without an additional primer coating	Dry mixed powder can be directly applied onto current collector and pressed into electrodes	97(NCM811)	2(Super P)	1(Parafilm® M)	146
	Styrene–butadiene rubber(SBR)	Graphite anode	(1) Sticky adhesive in high-pressure-based calendering (2) Elastic scaffold within the electrode	(1) Synthesizing graphite composite powder *via* freeze-drying (2) Calendering between the two rollers in the nip zone	95(natural graphite)	1[PTFE/Super P= 1/9(w/w)]	4(SBR)	132
	Sericin	Sulfur/carbon cathode	(1) High electrochemical stability at low potentials (2) Shear induced fibrillation enabling interconnection of active materials (3) Improve electrolyte wettability *via* polar functional groups	Fibrillation through DRYtraec® process	60(sulfur)	37(ketjen black)	3(sericin)	148

Table 2 *(continued)*

(b)

Classification		System	Function	Approach	Electrochemical performance						Ref.
					Loading level (mg cm^{-2})	Areal capacity(mAh cm^{-2})	Cell configuration	Voltage range	C-rate@ temperature	Capacity retention@cycle	
Dual binder	PTFE/PAA	NCM811 cathode	Improve adhesion and electrolyte wettability *via* polar functional groups of PAA	Twin-screw kneading of the mixed powder	30(NCM811)	~6	Graphite+Si/C||NCM811	2.5–4.25 V	1C@RT	82.2%@300 cycles (PTFE/PAA)/63.5%@300 cycles (PTFE)	90
	PTFE/High-gluten flour	NCM811, LCO cathode	Improve mechanical robustness *via* flour crosslinking	Hot-pressing of powder mixture	10(LCO) / 9.0 (NCM811)	~1.4 (LCO) / ~1.6 (NCM811)	Li metal||LCO /Li metal||NCM811	3.0–4.3 V /3.0–4.5 V	0.5C / 2C@RT	79.2%@560 cycle/ 80.3%@260 cycles	141
	PTFE/PAA-g-CMC	NCM622 cathode	(1) Anchoring PTFE to the electrode surface (2) Improve Li ion transport and adhesion	(1) Pre-anchoring of PAA-g CMC (2) binder onto NCM particles (3) PTFE-assisted fibrillation (4) Kneading and calendering	90(NCM622)	15.6	Graphite||NCM622	2.7–4.25 V	0.5C@25 °C	84%@50 cycles	145
	PTFE/PVdF	Graphite anode	Functional binder when PTFE decomposes in the first lithiation	(1) PVdF-assisted powder premixing (2) PTFE-induced fibrillation (3) Hot calendering (4) Lamination	15(graphite)	~4.6	Li metal||graphite	0.01–1.5 V	0.23mA cm^{-2}@RT	95%@50 cycles	149
	PTFE/PVP	Graphite anode	(1) Reducing PTFE decomposition (2) Enhancing mechanical robustness (3) Formation of a robust Li_3N-rich SEI layer	(1) Powder premixing (2) Kneading and calendering (3) Lamination	-	4.8 / 5.7	Li metal|graphite / graphite||NCM811	0.05–1.5 V /2.8–4.25 V	0.2C@25 °C	97.4%@100 cycles (PTFE/PVP), 94.3%@100 cycles (PTFE) / 93.0%@100 cycles (PTFE/PVP), 87.0%@100 cycles (PTFE)	142
	PTFE/CMC	Graphite anode	(1) Reducing PTFE decomposition (2) Improve Li ion transport and adhesion	Quasi-dry processing using ethanol to uniformly integrate CMC	30(graphite)	~10	Graphite||NCM811	2.7–4.3 V	0.5C@RT	48.96%@100 cycles (PTFE/CMC) 19.49%@100 cycles (PTFE)	143
PFAS-free	Phenoxy resin	NCM811 cathode	Formation of a continuous and ductile binder network	Hot-pressing a powder composite using a press machine	~40.0(NCM811)	~7.7	Li metal||NCM811	3.0–4.35 V	0.1C@25 °C	73.5%@50 cycles (dry phenoxy resin) 63.0%@50 cycles (wet phenoxy resin)	150
	Sacrificial binder (PP, paraffin wax, stearic acid)	LFP cathode	Rheological control and structural support during forming, followed by debinding to create a porous, high–active-material electrode	Powder extrusion molding (PEM) technology	—	13.7	Li metal||LFP	2.0–4.0 V	0.1C@20 °C	Good cyclability over 20 cycles	60
	Parafilm	NCM811 cathode	(1) Cost effectiveness (2) High electrochemical stability at low potentials (3) Providing natural adhesion without an additional primer coating	Dry mixed powder can be directly applied onto current collector and pressed into electrodes	36.8(NCM811)	6.6 (1st cycle)	Graphite||NCM811	3.0–4.3 V	0.3C@25 °C	63.1%@1000 cycles	146

Table 2 (*continued*)

(b)

Classification	System	Function	Approach	Electrochemical performance						Ref.
				Loading level (mg cm^{-2})	Areal capacity(mAh cm^{-2})	Cell configuration	Voltage range	C-rate@ temperature	Capacity retention@cycle	
Styrene–butadiene rubber(SBR)	Graphite anode	(1) Sticky adhesive in high-pressure-based calendering (2) Elastic scaffold within the electrode	(1) Synthesizing graphite composite powder *via* freeze-drying (2) Calendering between the two rollers in the nip zone	45(LFP)	5.6 (1st cycle)	Graphite||LFP	2.45–3.9 V	0.5C	74.6%@200 cycles	132
Sericin	Sulfur/carbon cathode	(1) High electrochemical stability at low potentials (2) Shear induced fibrillation enabling interconnection of active materials (3) Improve electrolyte wettability *via* polar functional groups	Fibrillation through DRY-trae$^{®}$ process	2.5 ± 0.2(sulfur)	—	Li metal||Sulfur	1.5–2.5 V	0.1C@25 ± 1 °C	836 mAh g^{-1}@50 cycles (sericin) 695 mAh g^{-1}@50 cycles (PTFE)	148

resulted in a wider electrochemical stability window, particularly at low potentials, while simultaneously addressing PFAS-related environmental and regulatory concerns. The successful fabrication of thick electrodes exceeding 5–9 mAh cm^{-2} along with long-term cycling stability underscores the fact that non-fibrillating, thermoplastic binders represent a viable and scalable alternative to PTFE-dominated DPE technologies. Similarly, Kim *et al.*[132] designed PFAS-free DPEs based on styrene–butadiene rubber (SBR), which acts as a sticky adhesive during high-pressure calendering. The resulting DPEs exhibited an open-channel interfacial structure that promoted the formation of a favorable SEI rich in LiF, thereby enhancing cycling stability even at an ultrahigh areal loading of 10.6 mAh cm^{-2}.

Collectively, the various dual-binder and beyond-PTFE (PFAS-free) binder systems reviewed in this section demonstrate that the challenges of DPE manufacturing can be addressed through multiple, function-oriented material design strategies rather than by relying on PTFE alone. To facilitate a systematic comparison, Table 2[60,90,132,141–143,145,146,148–150] summarizes representative binder systems with respect to their primary functional roles, the corresponding DPE fabrication approaches, and the resulting electrochemical performance, particularly in terms of capacity retention during cycling, thus providing a perspective on the effectiveness and scalability of emerging binder technologies for DPEs.

5. Summary and outlook: advanced materials and processes for scalable dry-processed electrode manufacturing

DPE manufacturing provides an alternative electrode fabrication route for LIBs by removing conventional solvent-dependent processing steps. As systematically reviewed in this paper, the primary advantages of dry processing (*i.e.*, environmental sustainability, reduced manufacturing cost, and high coating speed) originate from the elimination of solvent handling and drying steps. However, as schematically illustrated in Fig. 9, the practical application of DPEs critically depends on optimization at both the process and material levels.

Regarding processing perspectives, each step of DPE manufacturing, including powder mixing, kneading, sheet forming, laminating, and calendering, plays a critical role in determining the electrode microstructure. Non-uniform powder mixing leads to local heterogeneity in the distribution of binders and conductive additives, which subsequently manifests as spatial variations in electronic conductivity and mechanical strength. Similarly, insufficient or non-uniform PTFE fibrillation during kneading compromises the formation of a continuous fibrous binder network, resulting in poor cohesion within the bulk electrode, as well as weak adhesion at the electrode/current collector interface. Lamination and calendering, while essential for densification and interfacial contact, can introduce further constraints, such as crack formation and density gradients,

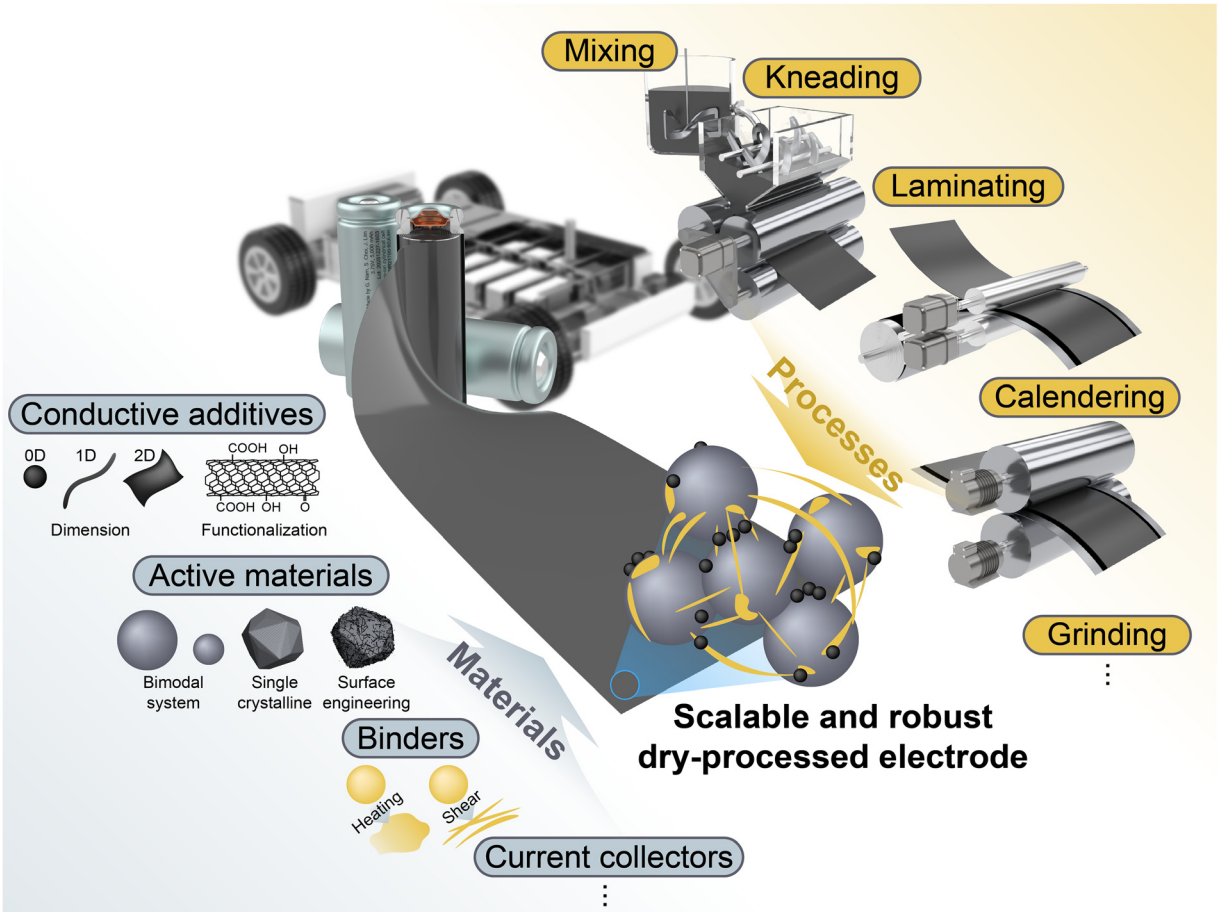

Fig. 9 Schematic illustration highlighting the interplay between material and process innovations essential for scalable manufacturing of high-performance, sustainable DPEs with distinct microstructural features.

when the mechanical compliance of the electrode film is not properly matched to the applied stress. These results show that process control plays a critical role in both microstructural stability and electrochemical performance.

Meanwhile, materials-level design also plays an important role in DPE performance. The fibrillation behavior of PTFE binders, for instance, is intrinsically related to the M_W, particle size, and crystallinity, which, in turn, determines the robustness of the fibrous network formed during shear-driven processing. Conductive additives with different dimensions and surface energies respond differently to dry mixing and kneading, influencing percolation pathways and contact resistance. Likewise, the choice of the active material or polymeric binder affects electrochemical stability and mechanical stress accommodation during lamination and calendering. Importantly, these material properties collectively define the processing window for obtaining uniform microstructures.

The intrinsic limitations of PTFE-based DPEs highlight the need for next-generation binder concepts. From a scale-up perspective, thicker and higher-loading DPE architectures may require higher absolute binder input to maintain mechanical integrity and processability, even when the binder fraction is controlled and optimized. This trend can amplify the environmental, recycling, and regulatory burden of fluorinated binder systems at the cell-manufacturing level. Therefore, future binder design should target not only fibrillation capability and electrode robustness but also reduced environmental impact and safer material pathways. In this context, dual-binder strategies—in which PTFE serves as a mechanically robust fibrillating scaffold while secondary polymers introduce complementary functions—demonstrate that key performance bottlenecks in DPEs can be effectively addressed through synergistic materials design. Emerging PTFE-lean or PTFE-free systems, including co-binder systems and non-fluorinated polymer networks, provide an important transition route. In particular, bio-derived fibrillar candidates such as cellulose nanofibers (CNFs)[89,91,169] and protein-based fibroin[170,171] are attracting attention due to their potential to form mechanically supportive networks while offering improved environmental compatibility. More broadly, beyond-PTFE (PFAS-free) systems—including fibrillating fluorine-free macromolecules and non-fibrillating thermoplastic binders—further indicate that mechanical cohesion and scalable dry processing can be achieved through fundamentally different mechanisms.

In summary, scalable and mechanically robust DPE manufacturing should be treated as an integrated material–process–

microstructure engineering problem. Only by simultaneously optimizing processing routes and materials design, while accounting for electrochemical performance, manufacturability, and sustainability, can DPEs realize their full potential as a cornerstone technology for next-generation battery manufacturing.

Author contributions

G. Nam: conceptualization, investigation, methodology, data curation, writing – original draft; J. Lim: conceptualization, investigation, visualization, writing – original draft; S. Choi: conceptualization, investigation, visualization, data curation, writing – original draft; S. C. Nam: funding acquisition, writing – review and editing; K. Hong: funding acquisition, writing – review and editing; J. Lee: funding acquisition, writing – review and editing; Y. M. Lee: conceptualization, supervision, project administration, funding acquisition, writing – original draft, writing – review and editing.

Conflicts of interest

There are no conflicts to declare.

Data availability

No primary research results, software, or code have been included, and no new data were generated or analyzed as part of this review.

Acknowledgements

This work was supported by the Korea Institute for Advancement of Technology (KIAT) grant funded by the Technology Innovation Program funded by the Ministry of Trade, Industry & Energy (MOTIE, Korea) (No. 2410009726 (RS-2025-00437259) and No. 2410010799 (RS-2025-00420590), HRD program for industrial innovation). This study was also supported by POSCO HOLDINGS, Korea. We also acknowledge the use of ChatGPT (version 5.2) solely for language editing purposes to improve linguistic quality and readability. The authors take full responsibility for the scientific content of the article and have carefully read and checked the manuscript to ensure technical accuracy.

Notes and references

1 T. L. Sheldon and R. Dua, *Energy Res. Soc. Sci.*, 2025, **127**, 104327.
2 A. Kumar, *Energy Storage*, 2024, **6**, e70000.
3 R. Schmuch, R. Wagner, G. Hörpel, T. Placke and M. Winter, *Nat. Energy*, 2018, **3**, 267–278.
4 A. Masias, J. Marcicki and W. A. Paxton, *ACS Energy Lett.*, 2021, **6**, 621–630.
5 J. Deng, C. Bae, A. Denlinger and T. Miller, *Joule*, 2020, **4**, 511–515.
6 Y. Liu, Y. Zhu and Y. Cui, *Nat. Energy*, 2019, **4**, 540–550.
7 A. Kwade, W. Haselrieder, R. Leithoff, A. Modlinger, F. Dietrich and K. Droeder, *Nat. Energy*, 2018, **3**, 290–300.
8 W. Li, Z. He, Y. Jie, F. Huang, Y. Chen, Y. Wang, W. Zhang, X. Zhu, R. Cao and S. Jiao, *Adv. Funct. Mater.*, 2024, **34**, 2406770.
9 H.-H. Ryu, H. H. Sun, S.-T. Myung, C. S. Yoon and Y.-K. Sun, *Energy Environ. Sci.*, 2021, **14**, 844–852.
10 Z. Liu, Y. Zhang, S. Pan, Y. Chen, K. Yang, S. Wu, M. Liu, L. Hu, S. Jiang, X. Wang, G. Wang and M. Yao, *Energy Environ. Sci.*, 2026, **15**, 883.
11 J. Zheng, M. S. Kim, Z. Tu, S. Choudhury, T. Tang and L. A. Archer, *Chem. Soc. Rev.*, 2020, **49**, 2701–2750.
12 N. Kim, Y. Kim, J. Sung and J. Cho, *Nat. Energy*, 2023, **8**, 921–933.
13 J. Li, J. Fleetwood, W. B. Hawley and W. Kays, *Chem. Rev.*, 2022, **122**, 903–956.
14 J. Lim, S. Park, H. Lee, S. Choi, G. Nam, K.-G. Kim, J. Choi, Y.-G. Lee and Y. M. Lee, *J. Energy Chem.*, 2025, **105**, 87–95.
15 J. Lim, K. Kang, S. Choi, M. Song, W. Yang, G. Nam, M. Kwon, R. Hong, D. Kang, H. Kim and Y. M. Lee, *Carbon Neutralization*, 2025, **4**, e70050.
16 J. Lim, D. Kang, C. Bak, S. Choi, M. Lee, H. Lee and Y. M. Lee, *Nano-Micro Lett.*, 2025, **18**, 75.
17 J. Kang, J. Lim, H. Lee, S. Park, C. Bak, Y. Shin, H. An, M. Lee, M. Lee, S. Lee, B. Choi, D. Kang, S. Chae, Y. M. Lee and H. Lee, *Adv. Sci.*, 2024, **11**, 2403071.
18 J. Wu, X. Zhang, Z. Ju, L. Wang, Z. Hui, K. Mayilvahanan, K. J. Takeuchi, A. C. Marschilok, A. C. West, E. S. Takeuchi and G. Yu, *Adv. Mater.*, 2021, **33**, 2101275.
19 Y. Kuang, C. Chen, D. Kirsch and L. Hu, *Adv. Energy Mater.*, 2019, **9**, 1901457.
20 H. Kang, J.-H. Kim, J. Lim, C. Heo, K.-S. Oh, H. Moon, S. Choi, J. Nam, Y. M. Lee and S.-Y. Lee, *ACS Energy Lett.*, 2025, **10**, 6223–6235.
21 Y. S. Zhang, N. E. Courtier, Z. Zhang, K. Liu, J. J. Bailey, A. M. Boyce, G. Richardson, P. R. Shearing, E. Kendrick and D. J. L. Brett, *Adv. Energy Mater.*, 2022, **12**, 2102233.
22 T. Lombardo, A. C. Ngandjong, A. Belhcen and A. A. Franco, *Energy Storage Mater.*, 2021, **43**, 337–347.
23 J. Entwistle, R. H. Ge, K. Pardikar, R. Smith and D. Cumming, *Renew. Sustain. Energy Rev.*, 2022, **166**, 112624.
24 Y. Liu, R. Zhang, J. Wang and Y. Wang, *iScience*, 2021, **24**, 102332.
25 T. Krüger, H. Gruhn, M. Mund, K. Dilger and M. W. Kandula, *Energy Technol.*, 2025, **13**, 2402221.
26 H. Liu, X. Cheng, Y. Chong, H. Yuan, J.-Q. Huang and Q. Zhang, *Particuology*, 2021, **57**, 56–71.
27 R. Sliz, J. Valikangas, H. Silva Santos, P. Vilmi, L. Rieppo, T. Hu, U. Lassi and T. Fabritius, *ACS Appl. Energ. Mater.*, 2022, **5**, 4047–4058.
28 S. Ahmed, P. A. Nelson, K. G. Gallagher and D. W. Dees, *J. Power Sources*, 2016, **322**, 169–178.

29 Y. H. Liang, H. Long, Z. M. Huang, T. He, X. M. Chen, M. Li, H. Chen and S. Q. Zhang, *Adv. Funct. Mater.*, 2025, e18619.
30 Y. Lu, C.-Z. Zhao, H. Yuan, J.-K. Hu, J.-Q. Huang and Q. Zhang, *Matter*, 2022, **5**, 876–898.
31 R. Tao, Y. Gu, Z. Du, X. Lyu and J. Li, *Nat. Rev. Clean Technol.*, 2025, **1**, 116–131.
32 W. Jin, G. Song, J.-K. Yoo, S.-K. Jung, T.-H. Kim and J. Kim, *ChemElectroChem*, 2024, **11**, e202400288.
33 Y. Bi, Q. Li, R. Yi and J. Xiao, *J. Electrochem. Soc.*, 2022, **169**, 020521.
34 F. Degen, M. Winter, D. Bendig and J. Tübke, *Nat. Energy*, 2023, **8**, 1284–1295.
35 H. Zhang, B. Xue, S. Li, Y. Yu, X. Li, Z. Chang, H. Wu, Y. Hu, K. Huang, L. Liu, L. Chen and Y. Su, *Sci. Rep.*, 2023, **13**, 7952.
36 D. L. Wood, J. D. Quass, J. Li, S. Ahmed, D. Ventola and C. Daniel, *Drying Technol.*, 2018, **36**, 234–244.
37 M. Abdollahifar, H. Cavers, S. Scheffler, A. Diener, M. Lippke and A. Kwade, *Adv. Energy Mater.*, 2023, **13**, 2300973.
38 S. Choi, J. P. Seo, J. Lim, C. B. Dzakpasu, Y. Roh, C. Bak, S. Kim, H. Lee and Y. M. Lee, *Batter. Supercaps*, 2025, **8**, e202400638.
39 J. Lim, J. Song, K.-G. Kim, J. K. Koo, H. Lee, D. Kang, Y.-J. Kim, J. Park and Y. M. Lee, *Small*, 2025, **21**, 2410485.
40 M. Ebner, D.-W. Chung, R. E. García and V. Wood, *Adv. Energy Mater.*, 2014, **4**, 1301278.
41 S. Hein, T. Danner, D. Westhoff, B. Prifling, R. Scurtu, L. Kremer, A. Hoffmann, A. Hilger, M. Osenberg, I. Manke, M. Wohlfahrt-Mehrens, V. Schmidt and A. Latz, *J. Electrochem. Soc.*, 2020, **167**, 013546.
42 T.-T. Nguyen, A. Demortière, B. Fleutot, B. Delobel, C. Delacourt and S. J. Cooper, *npj Comput. Mater.*, 2020, **6**, 123.
43 P. Mitchell, L. Zhong and X. Xi, *Recyclable dry particle based adhesive electrode and methods of making same*, *US Pat.*, US7342770B2, 2008.
44 M. Ank, A. Sommer, K. Abo Gamra, J. Schöberl, M. Leeb, J. Schachtl, N. Streidel, S. Stock, M. Schreiber, P. Bilfinger, C. Allgäuer, P. Rosner, J. Hagemeister, M. Rößle, R. Daub and M. Lienkamp, *J. Electrochem. Soc.*, 2023, **170**, 120536.
45 X. Han, M. R. Funk, F. Shen, Y.-C. Chen, Y. Li, C. J. Campbell, J. Dai, X. Yang, J.-W. Kim, Y. Liao, J. W. Connell, V. Barone, Z. Chen, Y. Lin and L. Hu, *ACS Nano*, 2014, **8**, 8255–8265.
46 M. Ryu, Y.-K. Hong, S.-Y. Lee and J. H. Park, *Nat. Commun.*, 2023, **14**, 1316.
47 M. E. Sotomayor, C. D. L. Torre-Gamarra, W. Bucheli, J. M. Amarilla, A. Varez, B. Levenfeld and J. Y. Sanchez, *J. Mater. Chem. A*, 2018, **6**, 5952–5961.
48 S. El Khakani, N. Verdier, D. Lepage, A. Prébé, D. Aymé-Perrot, D. Rochefort and M. Dollé, *J. Power Sources*, 2020, **454**, 227884.
49 S. Shiraki, H. Oki, Y. Takagi, T. Suzuki, A. Kumatani, R. Shimizu, M. Haruta, T. Ohsawa, Y. Sato, Y. Ikuhara and T. Hitosugi, *J. Power Sources*, 2014, **267**, 881–887.
50 J. Liu, B. Ludwig, Y. Liu, Z. Zheng, F. Wang, M. Tang, J. Wang, J. Wang, H. Pan and Y. Wang, *Adv. Mater. Technol.*, 2017, **2**, 1700106.
51 Y. Liu, X. Gong, C. Podder, F. Wang, Z. Li, J. Liu, J. Fu, X. Ma, P. Vanaphuti, R. Wang, A. Hitt, Y. Savsatli, Z. Yang, M. Ge, W.-K. Lee, B. Yonemoto, M. Tang, H. Pan and Y. Wang, *Joule*, 2023, **7**, 952–970.
52 H. Abe, A. Kondo, M. Naito, T. Wakimoto and M. Yamaguchi, *Electrostatic dry coating of cathode materials for Li ion battery*, in: 9th IMAPS/ACerS International Conference and Exhibition on Ceramic Interconnect and Ceramic Microsystems Technologies, CICMT 2013, Orlando, FL, 2013.
53 B. Trembacki, E. Duoss, G. Oxberry, M. Stadermann and J. Murthy, *J. Electrochem. Soc.*, 2019, **166**, A923.
54 R. W. Gore, Process for producing porous products, *US Pat.*, US3953566A, 1976.
55 H. Oh, G.-S. Kim, B. U. Hwang, J. Bang, J. Kim and K.-M. Jeong, *Chem. Eng. J.*, 2024, **491**, 151957.
56 H. Oh, G.-S. Kim, J. Bang, S. Kim and K.-M. Jeong, *Energy Environ. Sci.*, 2025, **18**, 645–658.
57 J. K. Koo, J. Lim, J. Shin, J. K. Seo, C. Ha, W. T. A. Ran, J.-H. Lee, Y. Kwon, Y. M. Lee and Y.-J. Kim, *Energy Storage Mater.*, 2025, **78**, 104270.
58 G.-T. Kim, G. B. Appetecchi, F. Alessandrini and S. Passerini, *J. Power Sources*, 2007, **171**, 861–869.
59 L. Helmers, L. Froböse, K. Friedrich, M. Steffens, D. Kern, P. Michalowski and A. Kwade, *Energy Technol.*, 2021, **9**, 2000923.
60 C. de la Torre-Gamarra, M. E. Sotomayor, J.-Y. Sanchez, B. Levenfeld, A. Várez, B. Laïk and J.-P. Pereira-Ramos, *J. Power Sources*, 2020, **458**, 228033.
61 L. Yuan, H. Liu and X. Jiang, *J. Energy Storage*, 2024, **90**, 111912.
62 D.-W. Park, N. A. Cañas, N. Wagner and K. A. Friedrich, *J. Power Sources*, 2016, **306**, 758–763.
63 M. Al-Shroofy, Q. Zhang, J. Xu, T. Chen, A. P. Kaur and Y.-T. Cheng, *J. Power Sources*, 2017, **352**, 187–193.
64 Z. Du, C. J. Janke, J. Li, D. L. Wood III and C. Daniel, *Method of solvent-free manufacturing of composite electrodes incorporating radiation curable binders*, *US Pat., US11289689B2*, 2022.
65 J. Park, H. Oh, J.-H. Lim, S. Jung, N. Yoo, J.-K. Yoo, K.-M. Jeong and K.-Y. Park, *Adv. Energy Mater.*, 2026, **16**, e04005.
66 C.-C. Chang, L.-J. Her, H.-K. Su, S.-H. Hsu and Y. T. Yen, *J. Electrochem. Soc.*, 2011, **158**, A481.
67 C.-C. Chang, H.-K. Su, L.-J. Her and J.-H. Lin, *J. Chin. Chem. Soc.*, 2012, **59**, 1233–1237.
68 Y. Kim, J. S. Hong, S. Y. Moon, J.-Y. Hong and J. U. Lee, *Carbon Lett.*, 2021, **31**, 1327–1337.
69 Y. J. Choi, E. J. C. Nacpil, J. Han, C. Zhu, I. S. Kim and I. Jeon, *Adv. Energy Sustain. Res.*, 2024, **5**, 2300219.
70 Q. Zhang, J.-Q. Huang, W.-Z. Qian, Y.-Y. Zhang and F. Wei, *Small*, 2013, **9**, 1237–1265.
71 B. Ludwig, Z. Zheng, W. Shou, Y. Wang and H. Pan, *Sci. Rep.*, 2016, **6**, 23150.

72 H. Kim, J. H. Lim, T. Lee, J. An, H. Kim, H. Song, H. Lee, J. W. Choi and J. H. Kang, *ACS Energy Lett.*, 2023, **8**, 3460–3466.
73 I. Hwang, K.-E. Sung, J. Hong, G.-S. Kang and J. Yoon, *Chem. Eng. J.*, 2025, **506**, 160159.
74 C. N. Thi Linh, V. D. Thuc, D. D. Mai, M. C. Nguyen, D. T. Pham, W. J. Yu and D. Kim, *Chem. Eng. J.*, 2025, **509**, 161183.
75 S. Z. Damnali, B. Villard, M. Leeb, B. Tekin, T. Woehrle, R. Daub, A. Hoffmann and M. Hoelzle, *J. Power Sources*, 2026, **663**, 238924.
76 K. Lee, Y. Jo, J. Seok Nam, H. Yu and Y.-J. Kim, *Chem. Eng. J.*, 2024, **487**, 150221.
77 J. Kim, K. Park, M. Kim, H. Lee, J. Choi, H. B. Park, H. Kim, J. Jang, Y.-H. Kim, T. Song and U. Paik, *Adv. Energy Mater.*, 2024, **14**, 2303455.
78 S. Jang, Y. Kang, H. Kim, J. Park and K. T. Lee, *Small Struct.*, 2025, **6**, 2400350.
79 J. Yoon, D. H. Kang, S. Shin, S. Yoo, H. Kim, J.-K. Lee, H.-J. Jin and Y. S. Yun, *Adv. Funct. Mater.*, 2025, e22855.
80 X. Shen, H. Yu, L. Ben, W. Zhao, Q. Wang, G. Cen, R. Qiao, Y. Wu and X. Huang, *J. Energy Chem.*, 2024, **90**, 133–143.
81 H. Choi, D. Moon, J. Sheem, J. K. Koo, S. Hong, S.-M. Oh and Y.-J. Kim, *J. Electrochem. Soc.*, 2023, **170**, 090511.
82 Z. Zhou, K. Lu, F. Chen, Y. Sun, X. Liu, Y. Niu, Y. Fan, X. Han and Y. Zheng, *J. Power Sources*, 2026, **666**, 239147.
83 J. Hong, J. Yoon, J.-W. Park, Y.-C. Ha, J. Lee and I. Hwang, *J. Power Sources*, 2025, **655**, 237925.
84 B. G. Meyer, G. Matthews, R. Scales, N. C. Mitchell, E. Darnbrough, R. A. House, D. E. J. Armstrong and P. S. Grant, *ACS Mater. Lett.*, 2025, **7**, 3444–3451.
85 Y.-J. Lee, S.-Y. Kim, W.-J. Song, J. Cha and D.-W. Kim, *Mater. Today Energy*, 2025, **51**, 101914.
86 D. Lee and A. Manthiram, *Small Methods*, 2023, **7**, 2201680.
87 D. J. Lee, J. Jang, J.-P. Lee, J. Wu, Y.-T. Chen, J. Holoubek, K. Yu, S.-Y. Ham, Y. Jeon, T.-H. Kim, J. B. Lee, M.-S. Song, Y. S. Meng and Z. Chen, *Adv. Funct. Mater.*, 2023, **33**, 2301341.
88 K.-H. Lee, H. Shim, S. H. Lee, H.-J. Kim, C. Park, J. Choi, S.-J. Lee, Y.-K. Hong, J. Lyu, J. C. Kim, S. Park, H. Cha, W. Jin, J. Kim, S. Choi, S.-Y. Lee, S.-K. Jung, M. De Volder, T.-H. Kim and G. Song, *Energy Environ. Sci.*, 2025, **18**, 8446–8461.
89 S. Jang, M.-H. Ryou, J.-Y. Bae, S.-H. Yu, S.-Y. Lee and J. Bang, *Prog. Polym. Sci.*, 2025, **166**, 101987.
90 K.-E. Sung, I. Hwang, J. Choi, S.-K. Jung and J. Yoon, *Chem. Eng. J.*, 2025, **511**, 161789.
91 N.-Y. Kim, J.-H. Kim, H. Koo, J. Oh, J.-H. Pang, K.-D. Kang, S.-S. Chae, J. Lim, K. W. Nam and S.-Y. Lee, *ACS Energy Lett.*, 2024, **9**, 5688–5703.
92 A. Komlev, D. Kudryavtseva, I. Neustroev, Y. Sudalenko, A. Altynnikov, A. Tsymbalyuk, A. Gagarin and R. Platonov, *Coatings*, 2025, **15**, 644.
93 Y. Li, Y. Zhou, Y. Gu, B. Chen, B. Wang, J. Yan, J. Liu, F. Chen, D. Zhao and X. Liu, *Vacuum*, 2022, **196**, 110763.
94 M. Nishino, Y. Okazaki, Y. Seto, T. Uehara, K. Endo, K. Yamamura and Y. Ohkubo, *Polymers*, 2022, **14**, 394.
95 M. W. Finnis, *J. Phys.: Condens. Matter*, 1996, **8**, 5811.
96 Y. Ye, R. Xu, W. Huang, H. Ai, W. Zhang, J. O. Affeld, A. Cui, F. Liu, X. Gao, Z. Chen, T. Li, X. Xiao, Z. Zhang, Y. Peng, R. A. Vila, Y. Wu, S. T. Oyakhire, H. Kuwajima, Y. Suzuki, R. Matsumoto, Y. Masuda, T. Yuuki, Y. Nakayama and Y. Cui, *Nat. Energy*, 2024, **9**, 643–653.
97 H. Li, L. Wang, Y. Song, Z. Zhang, H. Zhang, A. Du and X. He, *Adv. Funct. Mater.*, 2023, **33**, 2305515.
98 Y. Ye, L.-Y. Chou, Y. Liu, H. Wang, H. K. Lee, W. Huang, J. Wan, K. Liu, G. Zhou, Y. Yang, A. Yang, X. Xiao, X. Gao, D. T. Boyle, H. Chen, W. Zhang, S. C. Kim and Y. Cui, *Nat. Energy*, 2020, **5**, 786–793.
99 N. Li, J. Zhao, Y. Zhang, R. Song, N. Zhang, Y. Cui, J. Lin, H. Xu and Y. Huang, *Adv. Funct. Mater.*, 2025, **35**, 2419102.
100 F. Wang, S. Tang, Q. Han, S. Ji, J. Wang, B. Du, L. Xu, M. Guan, P. Lou, W. Zhang, Y.-C. Cao and S. Cheng, *J. Colloid Interface Sci.*, 2025, **678**, 57–65.
101 S. Y. Kim, T. K. Liu, H. S. Kim, D. H. Wang and J. H. Park, *Adv. Funct. Mater.*, 2025, e18597.
102 Z. Hu, R. Zhao, J. Yang, C. Wu and Y. Bai, *Energy Storage Mater.*, 2023, **59**, 102776.
103 T. Qin, H. Yang, Q. Li, X. Yu and H. Li, *Ind. Chem. Mater.*, 2024, **2**, 191–225.
104 J. Yoon, J. Lee, H. Kim, J. Kim and H.-J. Jin, *Polymers*, 2024, **16**, 254.
105 Y. Ohkubo, K. Ishihara, H. Sato, M. Shibahara, A. Nagatani, K. Honda, K. Endo and Y. Yamamura, *RSC Adv.*, 2017, **7**, 6432–6438.
106 M. Zhianmanesh, A. Gilmour, M. M. M. Bilek and B. Akhavan, *Appl. Phys. Rev.*, 2023, **10**, 021301.
107 J.-T. Kim, S. Kennedy, I. Phiri and S.-Y. Ryou, *ACS Appl. Mater. Interfaces*, 2024, **16**, 11400–11407.
108 M. Kanno and I. Honma, *J. Energy Storage*, 2025, **137**, 118658.
109 Y. Song, K. Gao, C. He, Y. Wu, S. Yang, N. Li, L. Yang, Y. Mao, W.-L. Song and H. Chen, *Appl. Energy*, 2023, **351**, 121904.
110 J. Zhang, H. Huang and J. Sun, *Powder Technol.*, 2022, **409**, 117828.
111 B. Schumm, A. Dupuy, M. Lux, C. Girsule, S. Dörfler, F. Schmidt, M. Fiedler, M. Rosner, F. Hippauf and S. Kaskel, *Adv. Energy Mater.*, 2025, **15**, 2406011.
112 A. Gyulai, W. Bauer and H. Ehrenberg, *ACS Appl. Energy Mater.*, 2023, **6**, 5122–5134.
113 G. A. B. Matthews, S. Wheeler, J. Ramírez-González and P. S. Grant, *Front. Energy Res.*, 2024, **11**, 1336344.
114 C. Wang, M. M. Thackeray and E. O. Fuller, *Integrated battery electrode fabrication using dry powder coating method*, *US Pat.*, US20150303481A1, 2015.
115 K. Raju, L. Wheatcroft, M. C. Lai, A. Mahadevegowda, L. F. J. Piper, C. Ducati, B. J. Inkson and M. De Volder, *J. Electrochem. Soc.*, 2024, **171**, 080519.
116 S. Hong, J. K. Seo, C. Ha, S.-M. Oh and Y.-J. Kim, *J. Power Sources*, 2025, **638**, 236621.

117 J. H. Kang, W. Jeong, M. S. Kang, H. W. Kim, D. W. Jeon, H. U. Lee, J. H. Hong, S. Han, M. Kim, S. Yang, D. Lee, P. J. Kim, T. Song, M. Yoon, L. Su, J. Choi and S. B. Cho, *Commun. Mater.*, 2025, **7**, 34.
118 W. Chung, H. Lee, J. Shim and J. H. Bang, *J. Electrochem. Sci. Technol.*, 2025, **16**, 512–520.
119 H.-s Kim, J. Y. Jung, K. Kim, C. Hwang, J. Yu, M.-S. Park and W. Cho, *Adv. Energy Mater.*, 2024, **14**, 2303965.
120 Y. Lyu, S. Dong, T. Zhang and Z.-S. Guo, *Eng. Fract. Mech.*, 2025, **321**, 111120.
121 J. Xu, B. Paredes-Goyes, Z. Su, M. Scheel, T. Weitkamp, A. Demortière and A. A. Franco, *Batter. Supercaps*, 2023, **6**, e202300371.
122 G. Matthews, B. Meyer, C. Doerrer, J. Ramírez-González, E. Darnbrough, N. Hallemans, D. Armstrong and P. S. Grant, *J. Mater. Chem. A*, 2025, **13**, 18283–18291.
123 T. J. Embleton, J. H. Choi, S.-J. Won, J. Ali, K. S. Saqib, K. Ko, M. Jo, J. Hwang, J. Park, J. H. Lee, J. Kim, M. K. Kim, J.-W. Jung, M. Park and P. Oh, *Energy Storage Mater.*, 2024, **71**, 103542.
124 R. Tao, B. Steinhoff, X.-G. Sun, K. Sardo, B. Skelly, H. M. Meyer, C. Sawicki, G. Polizos, X. Lyu, Z. Du, J. Yang, K. Hong and J. Li, *Chem. Eng. J.*, 2023, **471**, 144300.
125 K. Zhang, D. Li, X. Wang, J. Gao, H. Shen, H. Zhang, C. Rong and Z. Chen, *Materials*, 2024, **17**, 2349.
126 D. Kong, Q. Yang, Y. He and H. Hu, *ACS Appl. Energy Mater.*, 2025, **8**, 15438–15447.
127 S. Han, E.-H. Noh, S. Chae, K. Kwon, J. Lee, J.-S. Woo, S. Park, J. W. Lee, P. J. Kim, T. Song, W.-J. Kwak and J. Choi, *J. Energy Storage*, 2024, **96**, 112693.
128 S. Han, W. Jeong, R. Kang, M. Kim, M. Jeong, H.-W. Lee, Y.-J. An, H.-J. Ji, M. Yoon, P. J. Kim, S. Sun, T. Song, D. Lee, W.-J. Kwak and J. Choi, *EES Batteries*, 2025, **1**, 1267–1278.
129 Z. Wei, D. Kong, L. Quan, J. He, J. Liu, Z. Tang, S. Chen, Q. Cai, R. Zhang, H. Liu, K. Xu, L. Xing and W. Li, *Joule*, 2024, **8**, 1350–1363.
130 T. Lee, J. An, W. J. Chung, H. Kim, Y. Cho, H. Song, H. Lee, J. H. Kang and J. W. Choi, *ACS Appl. Mater. Interfaces*, 2024, **16**, 8930–8938.
131 Y. Zhao, Z. Liang, Y. Kang, Y. Zhou, Y. Li, X. He, L. Wang, W. Mai, X. Wang, G. Zhou, J. Wang, J. Li, N. Tavajohi and B. Li, *Energy Storage Mater.*, 2021, **35**, 353–377.
132 J. Kim, J. S. Park, J. J. Woo, S. Choi, J. Ma, J. Kim and S. Choi, *ACS Energy Lett.*, 2025, **10**, 2670–2678.
133 B. Chang, D. H. Yun, I. Hwang, J. K. Seo, J. Kang, G. Noh, S. Choi and J. W. Choi, *Adv. Mater.*, 2023, **35**, 2303787.
134 J. H. Kang, W. Jeong, M. S. Kang, H. W. Kim, D. W. Jeon, H. U. Lee, J. H. Hong, S. Han, M. Kim, S. Yang, D. Lee, P. J. Kim, T. Song, M. Yoon, L. Su, J. Choi and S. B. Cho, *Commun. Mater.*, 2025, **7**, 34.
135 J.-K. Hu, H. Yuan, S.-J. Yang, Y. Lu, S. Sun, J. Liu, Y.-L. Liao, S. Li, C.-Z. Zhao and J.-Q. Huang, *J. Energy Chem.*, 2022, **71**, 612–618.
136 W. Shin, D. S. Kwon, M. Kim, J. Woo, H. G. Jung, J. Bang, J. Shim and J. K. Yoo, *ChemSusChem*, 2025, e202501943.
137 L. Meng, B. Song, Y. Lu, K. Lv, W. Gao, Y. Wang and G. Jiang, *J. Environ. Sci.*, 2021, **107**, 77–86.
138 E. K. Savvidou, A. Rensmo, J. P. Benskin, S. Schellenberger, X. Hu, M. Weil and I. T. Cousins, *Environ. Sci. Technol.*, 2024, **58**, 21908–21917.
139 A. A. Dolatabad, X. Zhang, J. Mai, A. Kubátová, J. Cao and F. Xiao, *J. Hazard. Mater.*, 2025, **496**, 139322.
140 J. Kang, H. Eom, D. Yoo, M.-L. Seol, J. W. Han, H. Song, J. Li and I. Nam, *Energy Storage Mater.*, 2025, **82**, 104662.
141 R. He, W. Zhong, C. Cai, S. Li, S. Cheng and J. Xie, *Adv. Energy Mater.*, 2024, **14**, 2402109.
142 J. Lee, C. Y. Son, S. Han, S. Yang, P. J. Kim, D. Lee, J. W. Lee, W.-H. Ryu and J. Choi, *Chem. Eng. J.*, 2025, **503**, 158271.
143 C. Nguyen Thi Linh, V. Dong Thuc, T. A. Nguyen, T. D. Cam Ha and D. Kim, *Mater. Today Energy*, 2025, **54**, 102071.
144 M.-J. Kim, J.-H. Cha and E.-S. Oh, *J. Korean Battery Soc.*, 2024, **4**, 67–73.
145 J. Kang, H. Eom, S. Jang, D. Yoo, H. Lee, M. Kim, M.-L. Seol, J. W. Han, I. Nam and H. Song, *Adv. Mater.*, 2025, **37**, 2416872.
146 M. K. Kim, T. Yu, S. Jang, J. Lee, H. Oh, M. Jang, H. Cha, H. Lee, J. Kang, S. M. Lee, H. Shim, K.-H. Lee, G. Song, W. Jin, T.-H. Kim, S. Choi, K.-M. Jeong, J. T. Han, J.-K. Yoo, H.-G. Jung, S. Song, M. Park, J. Seong, D. Kim, H. Choi, M. Seong, M. J. Lim, W. R. Hwang, J. Nam, S. Jo and J. Kim, *Nat. Commun.*, 2025, **16**, 11174.
147 H.-M. Kim, B.-I. Yoo, J.-W. Yi, M.-J. Choi and J.-K. Yoo, *Nanomaterials*, 2022, **12**, 3320.
148 F. Schmidt, S. Kirchhoff, K. Jägle, A. De, S. Ehrling, P. Härtel, S. Dörfler, T. Abendroth, B. Schumm, H. Althues and S. Kaskel, *ChemSusChem*, 2022, **15**, e202201320.
149 Y. Zhang, S. Lu, F. Lou and Z. Yu, *Energy Technol.*, 2022, **10**, 2200732.
150 H. M. Kim, B. I. Yoo, J. W. Yi, M. J. Choi and J. K. Yoo, *Nanomaterials*, 2022, **12**, 3320.
151 J. U. Won, B. K. Park, J. Choi and K. J. Kim, *Adv. Energy Mater.*, 2025, **15**, e04841.
152 Y. H. Liang, H. Long, Z. M. Huang, T. He, X. M. Chen, M. Li, H. Chen and S. Q. Zhang, *Adv. Funct. Mater.*, 2025, e18619.
153 Y. Li, Y. Wu, Z. Wang, J. Xu, T. Ma, L. Chen, H. Li and F. Wu, *Mater. Today*, 2022, **55**, 92–109.
154 C. Y. Lim, G. Park and K. J. Lee, *Carbon Lett.*, 2025, **35**, 675–685.
155 Z. Ye, Z. Zou and C. Jiang, *Diamond Relat. Mater.*, 2023, **136**, 109911.
156 B. Kim, D. K. Kim, J. Yu and Y. Yoo, *Energy Environ. Mater.*, 2025, **8**, e70019.
157 R. Shvartzman-Cohen, Y. Levi-Kalisman, E. Nativ-Roth and R. Yerushalmi-Rozen, *Langmuir*, 2004, **20**, 6085–6088.

158 S. Mallakpour and S. Soltanian, *RSC Adv.*, 2016, **6**, 109916–109935.
159 M. Maugey, W. Neri, C. Zakri, A. Derre, A. Penicaud, L. Noe, M. Chorro, P. Launois, M. Monthioux and P. Poulin, *J. Nanosci. Nanotechnol.*, 2007, **7**, 2633–2639.
160 H. Lee, J. Park, H. Cho, J. Lee and K.-H. Lee, *RSC Adv.*, 2021, **11**, 38152–38160.
161 M. Hattori, T. Kiyono, Z. Zhao, M. Higashi, M. Fujishiro, Y. Kishikawa, J. Escorihuela and N. Shibata, *Nat. Commun.*, 2025, **17**, 669.
162 W. Yu, L. Chen, X. Zhang, R. Lu, X. Zhu and F. Lu, *Resour. Conserv. Recy.*, 2025, **215**, 108143.
163 S. Liu, R. J. Letcher, M. L. Diamond, A. Blum and D. Chen, *Nat. Commun.*, 2025, **17**, 108.
164 F. Xiao, B. Deng, D. Dionysiou, T. Karanfil, K. O'Shea, P. Roccaro, Z. J. Xiong and D. Zhao, *Nat. Water.*, 2023, **1**, 1004–1015.
165 L. Qiu, Z. Shao, D. Wang, F. Wang, W. Wang and J. Wang, *Carbohydr. Polym.*, 2014, **112**, 532–538.
166 P. Parikh, M. Sina, A. Banerjee, X. Wang, M. S. D'Souza, J.-M. Doux, E. A. Wu, O. Y. Trieu, Y. Gong, Q. Zhou, K. Snyder and Y. S. Meng, *Chem. Mater.*, 2019, **31**, 2535–2544.
167 I. İ. Avcı Yayla, N. Yuca, E. Sezer and B. Ustamehmetoğlu, *Energy Storage*, 2022, **4**, e338.
168 S. Choi, T.-w Kwon, A. Coskun and J. W. Choi, *Science*, 2017, **357**, 279–283.
169 Y.-K. Hong, J.-H. Kim, N.-Y. Kim, K.-S. Oh, H.-I. Kim, S. Ryu, Y. Ko, J.-Y. Kim, K.-H. Lee and S.-Y. Lee, *Nano-Micro Lett.*, 2025, **17**, 112.
170 Y. Guo, R. Soni, K. Coke, J. B. Robinson, F. Iacoviello, R. S. Young, R. Jervis, P. R. Shearing and T. S. Miller, *ACS Sustain. Chem. Eng.*, 2025, **13**, 13726–13739.
171 P. Dong, X. Zhang, J. Zamora, J. McCloy and M.-K. Song, *J. Energy Chem.*, 2023, **80**, 442–451.